Highlights

- Establishing analytical approaches to determine the overall size-dependent response of composites embedding general interfaces based on CSA and GSCM,
- Providing new bounds and estimates on the macroscopic properties of particulate composites together with the state of the stress and strain in each phase,
- Comparison with the literature on the topic and showing an excellent agreement and unification of available estimates,
- Introducing the two notions of ultimate bounds and size-dependent bounds.

Homogenization accounting for size effects in particulate composites due to general interfaces

Soheil Firooz[a], George Chatzigeorgiou[b], Fodil Meraghni[b], Ali Javili[a,*]

[a]*Department of Mechanical Engineering, Bilkent University, 06800 Ankara, Turkey*
[b]*LEM3-UMR 7239 CNRS, Arts et Metiers ParisTech Metz, 4 Rue Augustin Fresnel Metz 57078, France*

Abstract

Two analytical approaches are developed to determine the overall size-dependent response of composites embedding general interfaces. The first approach extends the composite sphere assemblage (CSA) approach and the generalized self-consistent method (GSCM) to account for the general interface model resulting in new bounds and estimates on the macroscopic properties of particulate composites. In the second approach, we develop an interface-enhanced Mori–Tanaka method that not only determines the effective properties but also provides the state of the stress and strain in each phase of the medium. The general interface model captures both elastic and cohesive interface models. Computational analysis is carried out using the finite element method to verify the analytical results. A remarkable agreement between the proposed analytical solutions and the computational results is obtained. A thorough parametric study is carried out to shed light on the role of the general interfaces in the overall behavior of composites. Motivated by the numerical and analytical findings, the material behavior is found to be bounded. Thus, two notions of *ultimate bounds* and *size-dependent bounds* are introduced and discussed.

Keywords: Homogenization, Imperfect interface, Size effects, Particulate composites, Mori–Tanaka method

1. Introduction

Almost all materials possess heterogeneous structures at certain length-scales. The overall behavior of heterogeneous materials can be determined from the response of their underlying micro-structures via the homogenization method pioneered by Hill (1963, 1972) and Ogden (1974). The classical homogenization method allows us to determine the overall behavior of composites based on the volume fraction, shape, orientation and distribution of their constituents. But classical homogenization cannot capture the *size effects*. As the characteristic length of a heterogeneous structure decreases e.g. in nano-composites, the effects of the surface and interface energy on the overall material response

*Corresponding author.
Email addresses: soheil.firooz@bilkent.edu.tr (Soheil Firooz), georges.chatzigeorgiou@ensam.eu (George Chatzigeorgiou), fodil.meraghni@ensam.eu (Fodil Meraghni), ajavili@bilkent.edu.tr (Ali Javili)

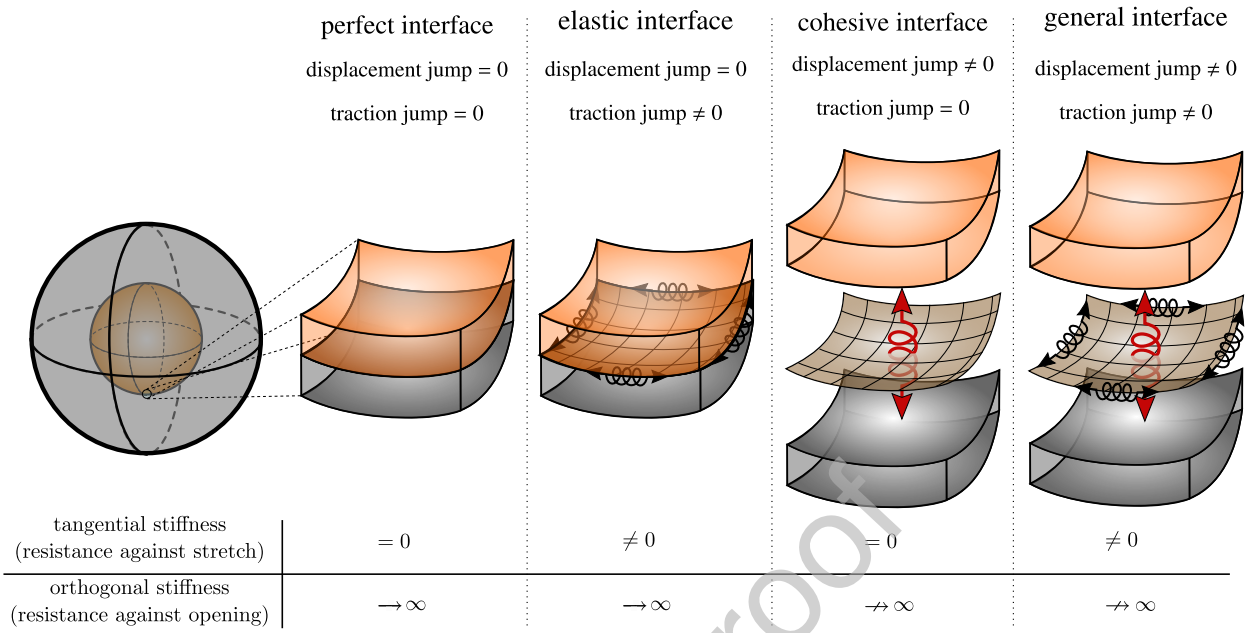

Figure 1: Categorization of interfaces based on the displacement and traction jumps. The perfect interface model is characterized by no displacement nor traction jumps. The elastic interface model allows for the traction jump but not for the displacement jump. The cohesive interface model assumes no traction jump across the interface whereas the displacement jump is permissible. All the interface models are unified in the general interface model where both displacement and traction jumps are permissible.

increases (Brisard et al., 2010; Chatzigeorgiou et al., 2015; Duan and Karihaloo, 2007; Duan et al., 2005; Fritzen and Leuschner, 2015; Javili et al., 2013a; Mogilevskaya et al., 2008; Monteiro et al., 2011; Nazarenko et al., 2017; Sharma, 2004; Sharma and Wheeler, 2007; Tian and Rajapakse, 2007; Yvonnet et al., 2008). Comparisons with experiments and atomistic simulations in (Davydov et al., 2013; Elsner et al., 2017; He and Lilley, 2008; Levitas and Samani, 2011; Olsson and Park, 2012; Park and Klein, 2008) justify that the size effects due to interfaces are physically meaningful. Emerging applications of nano-composites demand for better understanding of the interfacial effects on the overall response of heterogeneous media. In this contribution, we present two novel analytical methods to determine the overall behavior of *particulate composites* via a homogenization framework accounting for general interfaces. Furthermore, a computational analysis is carried out using the finite element method to verify the proposed analytical solutions. A two-dimensional counterpart of this work associated with *fiber composites* is only very recently published by Firooz et al. (2019a).

The term general interface here refers to a zero-thickness model allowing for both displacement and traction discontinuities across the interface (Hashin, 2001; Javili, 2017; Pham Huy and Sanchez-Palencia, 1974; Sanchez-Palencia, 1970). The bonding between the constituents of composites is important and can significantly influence the overall material response. The assumption of perfect bonding at interfaces is, in general, inadequate to describe the physical nature and mechanical behavior of the interface region and therefore, in many cases, an imperfect interface

model should be employed. Figure 1 categorizes the main interface models based on the continuity of the displacement or traction fields across the interface. The interface is referred to as perfect if both the displacement and traction jumps are zero. The elastic interface model allows for the traction jump whereas the displacement jump vanishes. The traction jump across the elastic interface is the result of the stress divergence along the interface conforming to a generalized Young–Laplace equation (Chen et al., 2006; Javili, 2018; Javili et al., 2013c). Interface elasticity theory spans a variety of studies from the fundamental works (Daher and Maugin, 1986; dell'Isola and Romano, 1987; Fried and Gurtin, 2007; Gurtin and Murdoch, 1975; Klarbring, 1991; Moeckel, 1975; Murdoch, 1976) and has been further investigated in (Altenbach and Eremeyev, 2011; Chhapadia et al., 2011; Cordero et al., 2016; Dingreville et al., 2014; Dingreville and Qu, 2008; Duan et al., 2009; Fedotov, 2018; Fried and Todres, 2005; Huang and Sun, 2007; Huang and Wang, 2006; Javili et al., 2013b; Liu et al., 2017; Steigmann and Ogden, 1999; Wang et al., 2010; Zhong and Meguid, 1997), among others. In the cohesive interface model the traction field is continuous across the interface unlike the displacement field. The cohesive interface model dates back to the seminal works (Barenblatt, 1959, 1962; Dugdale, 1960) and has been extensively studied in (Alfano and Crisfield, 2001; Brassart et al., 2009; Despringre et al., 2016; Dimitri et al., 2015; Fagerström and Larsson, 2006; Gasser and Holzapfel, 2003; Liu et al., 2019; Moës and Belytschko, 2002; Needleman, 1987; Ortiz and Pandolfi, 1999; Park and Paulino, 2011; Park et al., 2009; Qian et al., 2017; Remmers et al., 2008; van den Bosch et al., 2006; Wang et al., 2005; Wells and Sluys, 2001; Wu et al., 2016) from both analytical and computational aspects. The general interface model unifies all the aforementioned models allowing for both traction and displacement jumps. The general interface model has been examined in a seminal work of Hashin (2002) and further studied in (Benveniste, 2006; Benveniste and Miloh, 2001; Chatzigeorgiou et al., 2017; Firooz and Javili, 2019; Gu et al., 2014, 2011; Koutsawa et al., 2018; Monchiet and Bonnet, 2010) among others.

The term *size* here refers to the physical size of the micro-structure. The definition of the size is schematically illustrated in Fig. 2. The radii of the inclusion and the matrix can be calculated for a given volume fraction f and size ℓ. Throughout the manuscript, the macroscopic quantities are distinguished from their microscopic counterparts by a left superscript "M". That is, ${}^{\mathrm{M}}\{\bullet\}$ is a quantity at the macro-scale with its microscopic counterpart being $\{\bullet\}$. Moreover, quantities referring to the interface are distinct from the bulk quantities by a bar placed on top them. For instance, $\{\overline{\bullet}\}$ refers to an interface quantity with its bulk counterpart $\{\bullet\}$. The average and the jump of a quantity $\{\bullet\}$ across the interface are denoted by $\langle\!\langle\{\bullet\}\rangle\!\rangle$ and $[\![\{\bullet\}]\!]$, respectively.

The rest of the manuscript is organized as follows. Section 2 provides a brief discussion on the governing equations and problem definition. The analytical approaches are presented in Section 3. First the preliminaries of the RVE problem for particulate composites are introduced briefly. Next, the generalized self-consistent method and composite sphere assemblage method are extended to account for interfaces. This is then followed by developing the new

interface-enhanced Mori–Tanaka approach to incorporate interface effects in particulate composites using the modified Eshelby's heterogeneity problem. In Section 4, the analytical and computational solutions are compared through a set of numerical examples. A thorough comparison between our methodology and available analytical estimates in the literature is provided in Section 5. Section 6 concludes our work and provides further outlooks for future studies.

2. Governing equations

The governing equations of a continua embedding a general interface are briefly discussed in this section. Note that for the sake of brevity, only the final form of the most essential equations are stated. Detailed derivations are available in (Chatzigeorgiou et al., 2017; Javili, 2017; Javili et al., 2017). Consider a continuum body that occupies the configuration ${}^{\mathrm{M}}\mathcal{B}$ at the macro-scale corresponding to a heterogeneous medium, as shown in Fig. 3, with its underlying simplified representative volume element (RVE) at the micro-scale denoted as $\mathcal{B}$. In a computational homogenization framework, a proper RVE must be chosen such that (i) it is large enough to contain adequate details about the micro-structure and (ii) it is small enough to guarantee the scale separation (Gitman et al., 2005; Khisaeva and Ostoja-Starzewski, 2006; Temizer and Zohdi, 2007). In analytical homogenization, the RVE is often replaced by a spherical micro-structure suitable to represent isotropic particulate composites. At the micro-scale, the constitutive behavior of each phase is assumed to be known and the overall macroscopic material response is obtained via solving the associated boundary value problem and proper averaging over the RVE (Charalambakis et al., 2018; Kanouté et al., 2009; Matouš et al., 2017; Pindera et al., 2009; Saeb et al., 2016). As shown in Fig 3, we approximate the finite-thickness interphase between the constituents by the zero-thickness general interface model. The interface $\mathcal{I}$, splits the micro-structure into two disjoint subdomains $\mathcal{B}^+$ and $\mathcal{B}^-$ associated with the plus and minus sides of the interface,

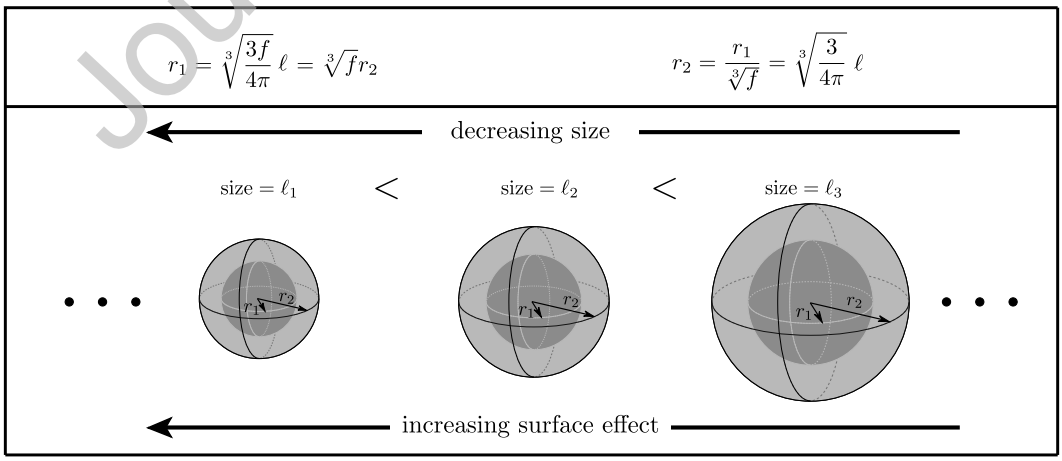

Figure 2: Illustration of the term "size". Using the volume fraction, the radii of the inclusion and the matrix can be obtained for each specific size. As a result, size is proportional to the radius of the inclusion or that of the matrix.

respectively. The unit normals to the external boundary and to the interface are denoted as $\boldsymbol{n}$ and $\overline{\boldsymbol{n}}$, respectively. Note, the interface unit normal points from the minus side of the interface to its plus side. Let $\boldsymbol{u}$ denote the displacement field in the bulk. The interface displacement $\overline{\boldsymbol{u}}$ is defined by the average displacement across the interface $\{\!\{\boldsymbol{u}\}\!\}$. The displacement average and the displacement jump across the interface are defined by

$$\{\!\{\boldsymbol{u}\}\!\} := \tfrac{1}{2}\left[\boldsymbol{u}^{+} + \boldsymbol{u}^{-}\right] \qquad \text{and} \qquad [\![\boldsymbol{u}]\!] := \boldsymbol{u}^{+} - \boldsymbol{u}^{-}\,, \tag{1}$$

where $\boldsymbol{u}^{+}$ and $\boldsymbol{u}^{-}$ are the displacement of the plus and minus side of the interface, respectively. It is worth noting that the above average considers only the displacements at the two edges of the interface, namely u^{+} and u^{-}, and does not stand for a classical volume average commonly used in homogenization approaches. The symmetric strain fields in the bulk and on the interface read

$$\boldsymbol{\varepsilon} = \frac{1}{2}\left[\boldsymbol{i}\cdot\operatorname{grad}\boldsymbol{u} + [\operatorname{grad}\boldsymbol{u}]^{\mathrm{t}}\cdot\boldsymbol{i}\right] \quad \text{in } \mathcal{B} \qquad \text{and} \qquad \overline{\boldsymbol{\varepsilon}} = \frac{1}{2}\left[\overline{\boldsymbol{i}}\cdot\overline{\operatorname{grad}}\,\overline{\boldsymbol{u}} + \left[\overline{\operatorname{grad}}\,\overline{\boldsymbol{u}}\right]^{\mathrm{t}}\cdot\overline{\boldsymbol{i}}\right] \quad \text{on } \mathcal{I}\,, \tag{2}$$

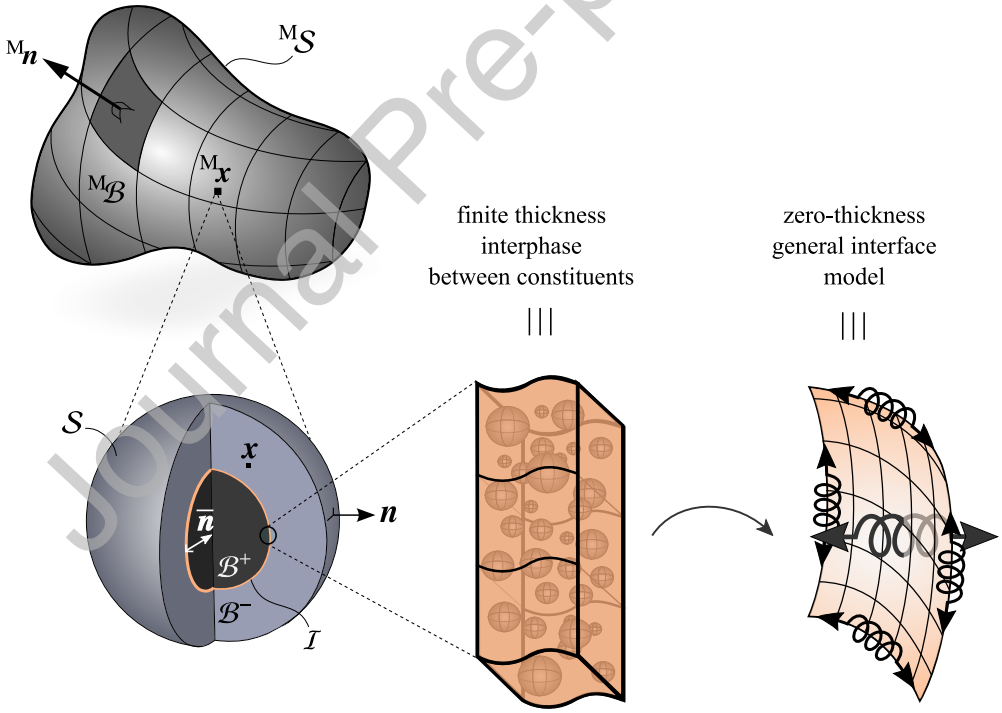

Figure 3: Problem definition for homogenization including the general interface model. The macro-structure is shown with its underlying RVE. The constitutive laws at the micro-scale are assumed to be known and the macroscopic behavior is obtained via solving the boundary value problem at the micro-scale. A finite-thickness interphase is replaced with a zero-thickness interface model. The classical interface models cannot capture heterogeneous material layer and thus, the general interface model is required.

in which $\boldsymbol{i}$ is the identity tensor. The operator $\overline{\text{grad}}\{\bullet\}$ characterizes the gradient projection onto the interface as $\overline{\text{grad}}\{\bullet\} = \text{grad}\{\bullet\} \cdot \overline{\boldsymbol{i}}$ in which the interface identity tensor reads $\overline{\boldsymbol{i}} = \boldsymbol{i} - \overline{\boldsymbol{n}} \otimes \overline{\boldsymbol{n}}$.

The total energy of the medium consists of the free energy density in the bulk ψ and on the interface $\overline{\psi}$. The free energy density in the bulk is assumed to be only a function of the bulk strain $\psi = \psi(\boldsymbol{\varepsilon})$ whereas the interface free energy density depends on both the interface strain and interface displacement jump as $\overline{\psi} = \overline{\psi}(\overline{\boldsymbol{\varepsilon}}, [\![\boldsymbol{u}]\!])$. The contributions of the interface curvature or higher gradients of the interface strain are not taken into account in this study. The constitutive relations in the bulk and on the interface in terms of their free energy densities read

$$\boldsymbol{\sigma} := \frac{\partial \psi}{\partial \boldsymbol{\varepsilon}} \quad \text{in } \mathcal{B}, \qquad \overline{\boldsymbol{\sigma}} := \frac{\partial \overline{\psi}}{\partial \overline{\boldsymbol{\varepsilon}}} \quad \text{and} \quad \overline{\boldsymbol{t}} := \frac{\partial \overline{\psi}}{\partial [\![\boldsymbol{u}]\!]} \quad \text{on } \mathcal{I}, \tag{3}$$

with $\overline{\boldsymbol{t}}$ being the interface traction and $\overline{\boldsymbol{t}} = \{\!\{\boldsymbol{\sigma}\}\!\} \cdot \overline{\boldsymbol{n}}$. In the absence of external forces, the balance equations in the bulk and on the interface read

$$\text{bulk} \begin{cases} \text{div}\boldsymbol{\sigma} = \boldsymbol{0} & \text{in } \mathcal{B}, \\ \boldsymbol{\sigma} \cdot \boldsymbol{n} = \boldsymbol{t} & \text{on } \mathcal{S}, \end{cases} \qquad \text{interface} \begin{cases} \overline{\text{div}}\,\overline{\boldsymbol{\sigma}} + [\![\boldsymbol{\sigma}]\!] \cdot \overline{\boldsymbol{n}} = \boldsymbol{0} & \text{along } \mathcal{I}, \\ \{\!\{\boldsymbol{\sigma}\}\!\} \cdot \overline{\boldsymbol{n}} = \overline{\boldsymbol{t}} & \text{across } \mathcal{I}, \end{cases} \tag{4}$$

where $\boldsymbol{t}$ is the traction on the boundary $\mathcal{S}$. Note, the interface curvature operator is embedded within the interface divergence operator $\overline{\text{div}}\{\bullet\} = \text{grad}\{\bullet\} : \overline{\boldsymbol{i}}$. The bulk material response is assumed to be standard and isotropic elastic taking the form $\boldsymbol{\sigma} = 2\mu\boldsymbol{\varepsilon} + \lambda\,[\boldsymbol{\varepsilon} : \boldsymbol{i}]\,\boldsymbol{i}$ where λ and μ are the Lamé parameters. For the interface, we additively decompose the material response into an orthogonal response across the interface and a tangential response along the interface

$$\overline{\boldsymbol{t}} = \overline{k}\,[\![\boldsymbol{u}]\!] \qquad \text{and} \qquad \overline{\boldsymbol{\sigma}} = 2\overline{\mu}\,\overline{\boldsymbol{\varepsilon}} + \overline{\lambda}\left[\overline{\boldsymbol{\varepsilon}} : \overline{\boldsymbol{i}}\right]\overline{\boldsymbol{i}}, \tag{5}$$

respectively, with $\overline{\lambda}$ and $\overline{\mu}$ being the interface Lamé parameters representing the interface resistance against in-plane stretches and $\overline{k}$ being the interface orthogonal resistance against opening.

Remark Usually, the interface parameters of zero-thickness interface models and the bulk parameters of an equivalent finite-thickness interphase are linked through the thickness of the interphase, see (Chatzigeorgiou et al., 2015; Duan et al., 2007; Gu et al., 2014; Hashin, 1991; Wang et al., 2005) for more details. The exact relations between these properties depend on the order of anisotropy and the type of imperfection of the interface model. As a general rule, the $\overline{\lambda}, \overline{\mu}$ are given by a combination of the equivalent interphase properties multiplied by the interphase thickness while $\overline{k}$ is proportional to the inverse of the thickness of the interphase.

Remark While not presented here, our methodology is, in principle, extensible for nonlinear interface conditions. The relations (5) can be adopted for nonlinear mechanisms, by considering field dependent $\overline{k}$, $\overline{\mu}$ and $\overline{\lambda}$, as well as proper evolution laws and activation criteria. Of course, a linearized incremental numerical scheme may be required (for instance, a return mapping algorithm approach) for introducing debonding or softening at the interface. An even more complex problem arises when the bulk materials are also nonlinear. In such cases, the non-uniformity of the fields inside each phase causes inconsistency in the validity of the analytical solutions provided in this manuscript. Various techniques can be employed to overcome such issues but they exceed the scopes of the current article and shall be studied in a separate contribution.

Equipped with the constitutive laws and the governing equations, we proceed with the micro to macro transition. In the classical computational homogenization framework, macroscopic quantities are related to their microscopic counterparts through volume averaging over the RVE. For this study, the classical definitions must be extended to incorporate the interfaces. The macroscopic stress and strain fields can be defined as surface integrals over the RVE's boundary as

$$ {}^{\mathrm{M}}\boldsymbol{\varepsilon} = \frac{1}{\mathscr{V}} \int_{\mathcal{S}} \frac{1}{2} \left[\boldsymbol{u} \otimes \boldsymbol{n} + \boldsymbol{n} \otimes \boldsymbol{u} \right] \mathrm{d}A \qquad \text{and} \qquad {}^{\mathrm{M}}\boldsymbol{\sigma} = \frac{1}{\mathscr{V}} \int_{\mathcal{S}} \boldsymbol{t} \otimes \boldsymbol{x} \, \mathrm{d}A \,, \tag{6} $$

that, using the extended divergence theorem Javili et al. (2017), simplify to

$$ {}^{\mathrm{M}}\boldsymbol{\varepsilon} = \frac{1}{\mathscr{V}} \int_{\mathcal{B}} \boldsymbol{\varepsilon} \, \mathrm{d}V + \frac{1}{\mathscr{V}} \int_{\mathcal{I}} \frac{1}{2} \left[[\![\boldsymbol{u}]\!] \otimes \overline{\boldsymbol{n}} + \overline{\boldsymbol{n}} \otimes [\![\boldsymbol{u}]\!] \right] \mathrm{d}A \qquad \text{and} \qquad {}^{\mathrm{M}}\boldsymbol{\sigma} = \frac{1}{\mathscr{V}} \int_{\mathcal{B}} \boldsymbol{\sigma} \, \mathrm{d}V + \frac{1}{\mathscr{V}} \int_{\mathcal{I}} \overline{\boldsymbol{\sigma}} \, \mathrm{d}A \,. \tag{7} $$

Next, an incremental energy equivalence, also known as the Hill–Mandel condition, between the scales is imposed in an extended form to account for the interface. The interface-enhanced Hill–Mandel condition reads

$$ \delta^{\mathrm{M}}\psi \overset{!}{=} \frac{1}{\mathscr{V}} \int_{\mathcal{B}} \delta\psi \, \mathrm{d}V + \frac{1}{\mathscr{V}} \int_{\mathcal{I}} \delta\overline{\psi} \, \mathrm{d}A \,, \tag{8} $$

where $\overset{!}{=}$ indicates that the equality is a condition. Employing the Hill's lemma, the Hill–Mandel condition (8) can be written as the boundary integral

$$ \int_{\mathcal{S}} \left[\delta\boldsymbol{u} - \delta^{\mathrm{M}}\boldsymbol{\varepsilon} \cdot \boldsymbol{x} \right] \cdot \left[\boldsymbol{t} - {}^{\mathrm{M}}\boldsymbol{\sigma} \cdot \boldsymbol{n} \right] \mathrm{d}A \overset{!}{=} 0 \,, \tag{9} $$

identifying suitable boundary conditions. Among all the boundary conditions satisfying the Hill-Mandel condition, the linear displacement boundary condition (DBC) and constant traction boundary condition (TBC) are imposed here.

This choice is necessary in order to have a meaningful comparison between the computational and analytical results. See Firooz et al. (2019b) for a comprehensive study on the effects of the boundary condition and the RVE type on the overall response of composites.

3. Analytical estimates

This section elaborates the two new analytical approaches that we develop here to determine the overall behavior of composites embedding general interfaces. The first approach is a direct extension of the composite sphere assemblage (CSA) approach and the generalized self-consistent method (GSCM) which incorporates the general interfaces providing bounds and estimates on the macroscopic properties. The second approach is a Mori–Tanaka-based approach in which the interaction tensors are calculated using the modified Eshelby's heterogeneity problem. The interaction tensors link the strain in the particle with the strain in the matrix.

Remark The case of long fiber composites with interface effects has been studied by the authors (Firooz et al., 2019a). For short fiber composites, however, analytical solutions to boundary value problems similar to the ones examined here are not available. Thus one should use other methods for studying them such as mean field, e.g. Mori-Tanaka. It is important to note that, the presence of the imperfect interface renders a nonuniform Eshelby tensor for interfaces with non-constant curvature (Sharma and Ganti, 2004) and therefore, certain simplifications and assumptions are unavoidable for short fiber composites. Dinzart and Sabar (2017) have applied a similar strategy for composites considering only the displacement jump at the interface by assuming that the stress field at the inclusion remains uniform, which is not generally true and accurate for imperfect interfaces.

3.1. Preliminaries of the RVE problem for particulate composites

Figure 4 shows a heterogeneous medium with its underlying micro-structure as well as a proper coordinate system to examine such medium. The simplified RVE consists of two concentric spheres corresponding to the matrix and the particle with the general interface lying at $r = r_1$. In passing, it proves convenient to express the homogenization problem in this medium in spherical coordinate system with the coordinates r, θ, ϕ. Throughout this manuscript, the quantities corresponding to the particle are designated by index 1 while index 2 indicates the matrix-related quantities. The volume fraction of the particle is $f = r_1^3/r_2^3$.

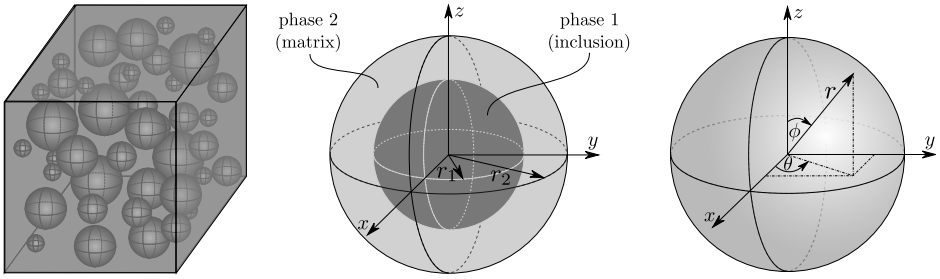

Figure 4: Heterogeneous medium (left) with its simplified RVE (middle) and the proper coordinate system (right) to examine such medium.

The constitutive material behavior in Voigt notation reads

$$\begin{bmatrix} \sigma_{rr} \\ \sigma_{\theta\theta} \\ \sigma_{\phi\phi} \\ \sigma_{r\theta} \\ \sigma_{r\phi} \\ \sigma_{\theta\phi} \end{bmatrix} = \begin{bmatrix} \kappa+4\mu/3 & \kappa-2\mu/3 & \kappa-2\mu/3 & 0 & 0 & 0 \\ \kappa-2\mu/3 & \kappa+4\mu/3 & \kappa-2\mu/3 & 0 & 0 & 0 \\ \kappa-2\mu/3 & \kappa-2\mu/3 & \kappa+4\mu/3 & 0 & 0 & 0 \\ 0 & 0 & 0 & \mu & 0 & 0 \\ 0 & 0 & 0 & 0 & \mu & 0 \\ 0 & 0 & 0 & 0 & 0 & \mu \end{bmatrix} \begin{bmatrix} \varepsilon_{rr} \\ \varepsilon_{\theta\theta} \\ \varepsilon_{\phi\phi} \\ 2\varepsilon_{r\theta} \\ 2\varepsilon_{r\phi} \\ 2\varepsilon_{\theta\phi} \end{bmatrix}, \quad \begin{aligned} \varepsilon_{rr} &= \frac{\partial u_r}{\partial r}, \\ \varepsilon_{\theta\theta} &= \frac{1}{r}\frac{\partial u_\theta}{\partial \theta} + \frac{u_r}{r}, \\ \varepsilon_{\phi\phi} &= \frac{1}{r\sin\theta}\frac{\partial u_\phi}{\partial \phi} + \frac{u_r}{r} + \frac{u_\theta \cos\theta}{r\sin\theta}, \\ 2\varepsilon_{r\phi} &= \frac{\partial u_\phi}{\partial r} + \frac{1}{r\sin\theta}\frac{\partial u_r}{\partial \phi} - \frac{u_\phi}{r}, \\ 2\varepsilon_{\theta\phi} &= \frac{1}{r}\frac{\partial u_\phi}{\partial \theta} + \frac{1}{r\sin\theta}\frac{\partial u_\theta}{\partial \phi} - \frac{u_\phi \cos\theta}{r\sin\theta}, \\ 2\varepsilon_{r\theta} &= \frac{\partial u_\theta}{\partial r} + \frac{1}{r}\frac{\partial u_r}{\partial \theta} - \frac{u_\theta}{r}, \end{aligned} \tag{10}$$

and the equilibrium equations in the bulk are

$$\begin{cases} \dfrac{\partial \sigma_{rr}}{\partial r} + \dfrac{1}{r}\dfrac{\partial \sigma_{r\theta}}{\partial \theta} + \dfrac{\sigma_{r\theta}\cos\theta}{r\sin\theta} + \dfrac{2\sigma_{rr} - \sigma_{\theta\theta} - \sigma_{\phi\phi}}{r} + \dfrac{1}{r\sin\theta}\dfrac{\partial \sigma_{r\phi}}{\partial \phi} = 0, \\ \dfrac{\partial \sigma_{r\theta}}{\partial r} + \dfrac{1}{r}\dfrac{\partial \sigma_{\theta\theta}}{\partial \theta} + \dfrac{3\sigma_{r\theta}}{r} + \dfrac{\left[\sigma_{\theta\theta} - \sigma_{\phi\phi}\right]\cos\theta}{r\sin\theta} + \dfrac{1}{r\sin\theta}\dfrac{\partial \sigma_{\theta\phi}}{\partial \phi} = 0, \\ \dfrac{\partial \sigma_{r\phi}}{\partial r} + \dfrac{1}{r}\dfrac{\partial \sigma_{\theta\phi}}{\partial \theta} + \dfrac{3\sigma_{r\phi}}{r} + \dfrac{2\sigma_{\theta\phi}\cos\theta}{r\sin\theta} + \dfrac{1}{r\sin\theta}\dfrac{\partial \sigma_{\phi\phi}}{\partial \phi} = 0. \end{cases} \tag{11}$$

Considering the spherical particles having the radius $r = r_1$, the constitutive relations at the interface read

$$\begin{bmatrix} \overline{\sigma}_{\theta\theta} \\ \overline{\sigma}_{\phi\phi} \\ \overline{\sigma}_{\theta\phi} \end{bmatrix} = \begin{bmatrix} \overline{\lambda}+2\overline{\mu} & \overline{\lambda} & 0 \\ \overline{\lambda} & \overline{\lambda}+2\overline{\mu} & 0 \\ 0 & 0 & \overline{\mu} \end{bmatrix} \begin{bmatrix} \overline{\varepsilon}_{\theta\theta} \\ \overline{\varepsilon}_{\phi\phi} \\ 2\overline{\varepsilon}_{\theta\phi} \end{bmatrix}, \quad \begin{aligned} \overline{\varepsilon}_{\theta\theta} &= \frac{1}{r_1}\frac{\partial \overline{u}_\theta}{\partial \theta} + \frac{\overline{u}_r}{r_1}, \\ \overline{\varepsilon}_{\phi\phi} &= \frac{1}{r_1\sin\theta}\frac{\partial \overline{u}_\phi}{\partial \phi} + \frac{\overline{u}_r}{r_1} + \frac{\overline{u}_\theta\cos\theta}{r_1\sin\theta}, \\ 2\overline{\varepsilon}_{\theta\phi} &= \frac{1}{r_1}\frac{\partial \overline{u}_\phi}{\partial \theta} + \frac{1}{r_1\sin\theta}\frac{\partial \overline{u}_\theta}{\partial \phi} - \frac{\overline{u}_\phi\cos\theta}{r_1\sin\theta}, \end{aligned} \quad \begin{bmatrix} \overline{t}_r \\ \overline{t}_\theta \\ \overline{t}_\phi \end{bmatrix} = \overline{k} \begin{bmatrix} [\![u_r]\!] \\ [\![u_\theta]\!] \\ [\![u_\phi]\!] \end{bmatrix}, \tag{12}$$

with the interface equilibrium equations

$$\left\{\begin{array}{l} -\dfrac{\overline{\sigma}_{\theta\theta}+\overline{\sigma}_{\phi\phi}}{r_1}+[\![\sigma_{rr}]\!]=0\,, \\ \dfrac{1}{r_1}\dfrac{\partial\overline{\sigma}_{\theta\theta}}{\partial\theta}+\dfrac{1}{r_1\sin\theta}\dfrac{\partial\overline{\sigma}_{\theta\phi}}{\partial\phi}+\dfrac{[\overline{\sigma}_{\theta\theta}-\overline{\sigma}_{\phi\phi}]\cos\theta}{r_1\sin\theta}+[\![\sigma_{r\theta}]\!]=0\,, \\ \dfrac{1}{r_1}\dfrac{\partial\overline{\sigma}_{\theta\phi}}{\partial\theta}+\dfrac{1}{r_1\sin\theta}\dfrac{\partial\overline{\sigma}_{\phi\phi}}{\partial\phi}+\dfrac{2\overline{\sigma}_{\theta\phi}\cos\theta}{r_1\sin\theta}+[\![\sigma_{r\phi}]\!]=0\,. \end{array}\right. \tag{13}$$

The displacements and stresses can be presented more precisely as

$$\begin{aligned} \boldsymbol{u} &= u_r\,\boldsymbol{n}_r+u_\theta\,\boldsymbol{n}_\theta+u_\phi\,\boldsymbol{n}_\phi\,, \\ \boldsymbol{\sigma} &= \sigma_{rr}\,\boldsymbol{n}_r\otimes\boldsymbol{n}_r+\sigma_{\theta\theta}\,\boldsymbol{n}_\theta\otimes\boldsymbol{n}_\theta+\sigma_{\phi\phi}\,\boldsymbol{n}_\phi\otimes\boldsymbol{n}_\phi+\frac{1}{2}\sigma_{r\theta}[\boldsymbol{n}_r\otimes\boldsymbol{n}_\theta+\boldsymbol{n}_\theta\otimes\boldsymbol{n}_r] \\ &\quad+\frac{1}{2}\sigma_{r\phi}[\boldsymbol{n}_r\otimes\boldsymbol{n}_\phi+\boldsymbol{n}_\phi\otimes\boldsymbol{n}_r]+\frac{1}{2}\sigma_{\theta\phi}[\boldsymbol{n}_\theta\otimes\boldsymbol{n}_\phi+\boldsymbol{n}_\phi\otimes\boldsymbol{n}_\theta]\,, \\ \overline{\boldsymbol{\sigma}} &= \overline{\sigma}_{\theta\theta}\,\boldsymbol{n}_\theta\otimes\boldsymbol{n}_\theta+\overline{\sigma}_{\phi\phi}\,\boldsymbol{n}_\phi\otimes\boldsymbol{n}_\phi+\frac{1}{2}\overline{\sigma}_{\theta\phi}[\boldsymbol{n}_\theta\otimes\boldsymbol{n}_z+\boldsymbol{n}_z\otimes\boldsymbol{n}_\theta]\,, \end{aligned} \tag{14}$$

with the normal vectors in spherical coordinates

$$\boldsymbol{n}_r=\begin{bmatrix}\sin\theta\cos\phi\\ \sin\theta\sin\phi\\ \cos\theta\end{bmatrix},\quad \boldsymbol{n}_\theta=\begin{bmatrix}\cos\theta\cos\phi\\ \cos\theta\sin\phi\\ -\sin\theta\end{bmatrix},\quad \boldsymbol{n}_\phi=\begin{bmatrix}-\sin\phi\\ \cos\phi\\ 0\end{bmatrix}. \tag{15}$$

Finally, the overall mechanical energy stored in the RVE and in equivalent homogeneous medium read

$$\begin{aligned} U^{\mathrm{RVE}} &= \frac{1}{2\mathscr{V}}\int_{\mathcal{B}}\boldsymbol{\sigma}:\boldsymbol{\varepsilon}\,\mathrm{d}V=\frac{3}{8\pi r_2}\int_0^{2\pi}\int_0^{\pi}\left[\sigma_{rr}^{(2)}u_r^{(2)}+\sigma_{r\theta}^{(2)}u_\theta^{(2)}+\sigma_{r\phi}^{(2)}u_\phi^{(2)}\right]_{r=r_2}\sin\theta\,\mathrm{d}\theta\,\mathrm{d}\phi\,, \\ U^{\mathrm{eq}} &= \frac{1}{2\mathscr{V}}\int_{\mathcal{B}}\boldsymbol{\sigma}:\boldsymbol{\varepsilon}\,\mathrm{d}V=\frac{3}{8\pi r_2}\int_0^{2\pi}\int_0^{\pi}\left[\sigma_{rr}^{\mathrm{eq}}u_r^{\mathrm{eq}}+\sigma_{r\theta}^{\mathrm{eq}}u_\theta^{\mathrm{eq}}+\sigma_{r\phi}^{\mathrm{eq}}u_\phi^{\mathrm{eq}}\right]_{r=r_2}\sin\theta\,\mathrm{d}\theta\,\mathrm{d}\phi\,. \end{aligned} \tag{16}$$

3.2. Composite sphere assemblage (CSA) approach and the generalized self-consistent method (GSCM)

The original CSA approach was developed by Hashin (1962) where he provided analytical solution strategies to estimate the macroscopic bulk modulus ${}^{\mathrm{M}}\kappa$ and the macroscopic shear modulus ${}^{\mathrm{M}}\mu$ of a particulate composite. While the original CSA approach can accurately calculate the effective bulk modulus, it can only provide bounds on the effective shear modulus. Christensen and Lo (1979) resolved this issue via solving the boundary value problem using the generalized self consistent method and obtained an estimation of the effective shear modulus. In this case, the RVE is assumed as a set of three concentric spheres where the external layer is an unknown effective medium. We extend these two approaches to account for the general interfaces and derive explicit expressions for the overall bulk modulus

${}^{\mathrm{M}}\kappa$ and semi-explicit expressions for the upper bound, lower bound and an estimate for the overall shear modulus ${}^{\mathrm{M}}\mu$ of particle reinforced composites.

3.2.1. Effective bulk modulus

Assume that the RVE is subject to a far field hydrostatic displacement field. The displacement in both Cartesian and spherical coordinates read

$$\boldsymbol{u}^0_{(x,y,z)} = \begin{bmatrix} \beta x \\ \beta y \\ \beta z \end{bmatrix} \quad \text{and} \quad \boldsymbol{u}^0_{(r,\theta,\phi)} = \begin{bmatrix} \beta r \\ 0 \\ 0 \end{bmatrix}. \tag{17}$$

For this type of boundary condition, Hashin (1962) has demonstrated that at every phase the displacement field that satisfies the equilibrium equations (11) reads

$$u_r^{(i)} = \beta r U_r^{(i)}(r), \quad u_\theta^{(i)} = u_\phi^{(i)} = 0 \qquad \text{with} \qquad U_r^{(i)}(r) = \Xi_1^{(i)} + \Xi_2^{(i)} \frac{1}{[r/r_1]^3}, \tag{18}$$

for $i = 1, 2$ where $i = 1$ corresponds to the particle and $i = 2$ corresponds to the matrix. The unknowns $\Xi_1^{(2)}$, $\Xi_2^{(2)}$, $\Xi_1^{(1)}$ and $\Xi_2^{(1)}$ can be calculated using the boundary and interface conditions

$$\begin{aligned}
&u_r^{(1)} \text{ finite at } r = 0 \quad \rightarrow \quad \Xi_2^{(1)} = 0, && \text{(finite displacement at } r = 0) \\
&\bar{t}_r = \bar{k}_r [\![u_r]\!] \quad \rightarrow \quad \frac{\sigma_{rr}^{(2)}(r_1) + \sigma_{rr}^{(1)}(r_1)}{2} = \bar{k}_r \left[u_r^{(2)}(r_1) - u_r^{(1)}(r_1)\right], && \text{(traction average at } r = r_1) \\
&\left[\overline{\operatorname{div}\sigma}\right]_r + [\![t_r]\!] = 0 \quad \rightarrow \quad -\frac{\overline{\sigma}_{\theta\theta} + \overline{\sigma}_{\phi\phi}}{r_1} + \sigma_{rr}^{(2)}(r_1) - \sigma_{rr}^{(1)}(r_1) = 0, && \text{(traction equilibrium at } r = r_1) \\
&u_r^{(2)}(r_2) = \beta r, && \text{(displacement at } r = r_2)
\end{aligned} \tag{19}$$

leading to the system

$$\begin{bmatrix} 1 + \dfrac{3\kappa_1}{2\bar{k}r_1} & -1 + \dfrac{3\kappa_2}{2\bar{k}r_1} & -1 - \dfrac{2\mu_2}{\bar{k}r_1} \\ 3\kappa_1 + \dfrac{2\left[\bar{\lambda} + \bar{\mu}\right]}{r_1} & -3\kappa_2 + \dfrac{2\left[\bar{\lambda} + \bar{\mu}\right]}{r_1} & 4\mu_2 + \dfrac{2\left[\bar{\lambda} + \bar{\mu}\right]}{r_1} \\ 0 & 1 & f \end{bmatrix} \begin{bmatrix} \Xi_1^{(1)} \\ \Xi_1^{(2)} \\ \Xi_2^{(2)} \end{bmatrix} = \begin{bmatrix} 0 \\ 0 \\ 1 \end{bmatrix}. \tag{20}$$

If the RVE is substituted by an equivalent homogeneous medium, applying the boundary condition (17) yields the displacement field $u_r^{\mathrm{eq}} = \beta r$ and $u_\theta^{\mathrm{eq}} = u_\phi^{\mathrm{eq}} = 0$. Using Eq. (16), the overall energy in both the RVE and the equivalent homogeneous medium read

$$U^{\mathrm{RVE}} = \frac{3\beta^2}{2}\left[3\kappa_2\Xi_1^{(2)} - 4f\mu_2\Xi_2^{(2)}\right] \qquad \text{and} \qquad U^{\mathrm{eq}} = \frac{9\beta^2}{2}{}^{\mathrm{M}}\kappa\,. \tag{21}$$

According to the Hill–Mandel condition, the above energies should be equal. Therefore, we obtain a closed-form expression for the macroscopic bulk modulus ${}^{\mathrm{M}}\kappa$ of particulate composites with general interfaces

$$\boxed{{}^{\mathrm{M}}\kappa = \frac{3\kappa_2\xi + 4\mu_2\eta}{3\left[\xi - f\eta\right]} \qquad \text{with} \qquad \begin{cases} \xi = \left[\dfrac{\overline{\lambda}+\overline{\mu}}{r_1} + \overline{k}r_1\right]\left[3\kappa_1 + 4\mu_2\right] + 4\overline{k}r_1\left[\dfrac{\overline{\lambda}+\overline{\mu}}{r_1}\right] + 12\kappa_1\mu_2\,, \\ \eta = \left[\dfrac{\overline{\lambda}+\overline{\mu}}{r_1} + \overline{k}r_1\right]\left[3\kappa_1 - 3\kappa_2\right] + 4\overline{k}r_1\left[\dfrac{\overline{\lambda}+\overline{\mu}}{r_1}\right] - 9\kappa_1\kappa_2\,. \end{cases}} \tag{22}$$

3.2.2. Strain bound on shear modulus

For this case, consider an RVE subject to a deviatoric displacement field. The displacement in both Cartesian and spherical coordinates read

$$\boldsymbol{u}^0_{(x,y,z)} = \begin{bmatrix} \beta y \\ -\beta x \\ 0 \end{bmatrix} \quad \text{and} \quad \boldsymbol{u}^0_{(r,\theta,\phi)} = \begin{bmatrix} \beta r \sin^2\theta\cos 2\phi \\ \beta r \sin\theta\cos\theta\cos 2\phi \\ -\beta r \sin\theta \sin 2\phi \end{bmatrix}. \tag{23}$$

For this type of boundary condition, Christensen and Lo (1979) have demonstrated that at every phase the displacement field that satisfies the equilibrium equations (11) reads

$$\begin{aligned} u_r^{(i)} &= \beta\, r\, U_r^{(i)}(r)\ \sin^2\theta\cos 2\phi\,, \\ u_\theta^{(i)} &= \beta\, r\, U_\theta^{(i)}(r)\ \sin\theta\cos\theta\cos 2\phi\,, \\ u_\phi^{(i)} &= -\beta\, r\, U_\theta^{(i)}(r)\ \sin\theta\sin 2\phi\,, \end{aligned} \quad \text{with} \quad \begin{cases} U_r^{(i)}(r) = \Xi_1^{(i)} + \left[2 - 3\dfrac{\kappa_i}{\mu_i}\right][r/r_1]^2\Xi_2^{(i)} + \dfrac{3\Xi_3^{(i)}}{[r/r_1]^5} + \left[3 + 3\dfrac{\kappa_i}{\mu_i}\right]\dfrac{\Xi_4^{(i)}}{[r/r_1]^3}\,, \\ U_\theta^{(i)}(r) = \Xi_1^{(i)} - \left[\dfrac{11}{3} + 5\dfrac{\kappa_i}{\mu_i}\right][r/r_1]^2\Xi_2^{(i)} - \dfrac{2\Xi_3^{(i)}}{[r/r_1]^5} + \dfrac{2\Xi_4^{(i)}}{[r/r_1]^3}\,. \end{cases} \tag{24}$$

The eight unknowns $\Xi_1^{(1)}$, $\Xi_2^{(1)}$, $\Xi_3^{(1)}$, $\Xi_4^{(1)}$, $\Xi_1^{(2)}$, $\Xi_2^{(2)}$, $\Xi_3^{(2)}$, $\Xi_4^{(2)}$ can be calculated using the boundary and interface conditions

$$
\begin{aligned}
&u_r^{(1)}, u_\theta^{(1)} \text{ finite at } r = 0 && \rightarrow \quad \Xi_3^{(1)} = \Xi_4^{(1)} = 0\,, && \text{finite displacement at } r = 0\\
&\bar{t}_r = \bar{k}_r \left[\!\left[u_r\right]\!\right] && \rightarrow \quad \sigma_{rr}^{(2)}(r_1) + \sigma_{rr}^{(1)}(r_1) = 2\bar{k}_r \left[u_r^{(2)}(r_1) - u_r^{(1)}(r_1)\right], && \text{(traction average at } r = r_1)\\
&\bar{t}_\theta = \bar{k}_\theta \left[\!\left[u_\theta\right]\!\right] && \rightarrow \quad \sigma_{r\theta}^{(2)}(r_1) + \sigma_{r\theta}^{(1)}(r_1) = 2\bar{k}_\theta \left[u_\theta^{(2)}(r_1) - u_\theta^{(1)}(r_1)\right], && \text{(traction average at } r = r_1)\\
&\left[\overline{\operatorname{div}\,\sigma}\right]_r + \left[\!\left[t_r\right]\!\right] = 0 && \rightarrow \quad -\frac{\overline{\sigma}_{\theta\theta} + \overline{\sigma}_{\phi\phi}}{r_1} + \sigma_{rr}^{(2)}(r_1) - \sigma_{rr}^{(1)}(r_1) = 0\,, && \text{(traction equilibrium at } r = r_1)\\
&\left[\overline{\operatorname{div}\,\sigma}\right]_\theta + \left[\!\left[t_\theta\right]\!\right] = 0 && \rightarrow \quad \frac{1}{r_1}\frac{\partial \overline{\sigma}_{\theta\theta}}{\partial \theta} + \frac{1}{r_1 \sin\theta}\frac{\partial \overline{\sigma}_{\theta\phi}}{\partial \phi} + \frac{[\overline{\sigma}_{\theta\theta} - \overline{\sigma}_{\phi\phi}]\cos\theta}{r_1 \sin\theta} && \text{(traction equilibrium at } r = r_1)\\
& && \qquad + \sigma_{r\theta}^{(2)}(r_1) - \sigma_{r\theta}^{(1)}(r_1) = 0\,, &&\\
&u_r^{(2)}(r = r_2) = \beta r \sin^2\theta \cos 2\phi\,, && u_\theta^{(2)}(r = r_2) = \beta r \sin\theta \cos\theta \cos 2\phi\,, && \text{(displacement at } r = r_2)
\end{aligned}
\tag{25}
$$

Further details regarding the construction of the system of equations are available in Appendix A.1. If the RVE is substituted by an equivalent homogeneous medium, applying the same boundary condition leads to the displacement field

$$
u_r^{\mathrm{eq}} = \beta r \sin^2\theta \cos 2\phi\,, \quad u_\theta^{\mathrm{eq}} = \beta r \sin\theta \cos\theta \cos 2\phi\,, \quad u_\phi^{\mathrm{eq}} = -\beta r \sin\theta \sin 2\phi\,. \tag{26}
$$

Equipped with all the displacement and stress fields, the overall energy according to Eq. (16) in both RVE and the equivalent homogeneous medium read

$$
U^{\mathrm{RVE}} = \frac{\beta^2}{5}\left[10\mu_2\Xi_1^{(2)} - 14\left[3\kappa_2 + \mu_2\right] f^{-2/3}\Xi_2^{(2)} - 2\left[9\kappa_2 + 8\mu_2\right] f\Xi_4^{(2)}\right] \qquad \text{and} \qquad U^{\mathrm{eq}} = 2\beta^{2\mathrm{M}}\mu\,. \tag{27}
$$

Considering $U^{\mathrm{RVE}} = U^{\mathrm{eq}}$ results in a *semi-explicit* expression for the strain bound on the macroscopic shear modulus

$$
{}^{\mathrm{M}}\mu_{\mathrm{strain}} = \frac{1}{10}\left[10\mu_2\Xi_1^{(2)} - 14\left[3\kappa_2 + \mu_2\right] f^{-2/3}\Xi_2^{(2)} - 2\left[9\kappa_2 + 8\mu_2\right] f\Xi_4^{(2)}\right], \tag{28}
$$

where $\Xi_1^{(2)}$, $\Xi_2^{(2)}$ and $\Xi_4^{(2)}$ are the solutions of the system of equations (A.1).

3.2.3. Stress bound on shear modulus

In order to obtain the stress bound, unlike the strain bound due to prescribed displacements, we prescribe traction on the RVE. Hence, consider an RVE subject to the traction field

$$\boldsymbol{t}^0_{(r,\theta,\phi)} = \begin{bmatrix} \sigma^0_{rr} \\ \sigma^0_{r\theta} \\ \sigma^0_{r\phi} \end{bmatrix} = \begin{bmatrix} \beta \sin^2\theta \cos 2\phi \\ \beta \sin\theta \cos\theta \cos 2\phi \\ -\beta \sin\theta \sin 2\phi \end{bmatrix}. \tag{29}$$

The solution of the boundary value problem for this case is similar to Eq. (24) and the eight unknowns $\Xi^{(1)}_1$, $\Xi^{(1)}_2$, $\Xi^{(1)}_3$, $\Xi^{(1)}_4$, $\Xi^{(2)}_1$, $\Xi^{(2)}_2$, $\Xi^{(2)}_3$ and $\Xi^{(2)}_4$ can be calculated using the boundary and interface conditions

$$\begin{aligned}
&u^{(1)}_r, u^{(1)}_\theta \text{ finite at } r = 0 && \rightarrow && \Xi^{(1)}_3 = \Xi^{(1)}_4 = 0\,, && \text{(finite displacement at } r = 0) \\
&\bar{t}_r = \bar{k}_r \llbracket u_r \rrbracket && \rightarrow && \sigma^{(2)}_{rr}(r_1) + \sigma^{(1)}_{rr}(r_1) = 2\bar{k}_r \left[u^{(2)}_r(r_1) - u^{(1)}_r(r_1) \right], && \text{(traction average at } r = r_1) \\
&\bar{t}_\theta = \bar{k}_\theta \llbracket u_\theta \rrbracket && \rightarrow && \sigma^{(2)}_{r\theta}(r_1) + \sigma^{(1)}_{r\theta}(r_1) = 2\bar{k}_\theta \left[u^{(2)}_\theta(r_1) - u^{(1)}_\theta(r_1) \right], && \text{(traction average at } r = r_1) \\
&\left[\overline{\operatorname{div}\,\overline{\sigma}} \right]_r + \llbracket t_r \rrbracket = 0 && \rightarrow && -\frac{\overline{\sigma}_{\theta\theta} + \overline{\sigma}_{\phi\phi}}{r_1} + \sigma^{(2)}_{rr}(r_1) - \sigma^{(1)}_{rr}(r_1) = 0\,, && \text{(traction equilibrium at } r = r_1) \\
&\left[\overline{\operatorname{div}\,\overline{\sigma}} \right]_\theta + \llbracket t_\theta \rrbracket = 0 && \rightarrow && \frac{1}{r_1}\frac{\partial \overline{\sigma}_{\theta\theta}}{\partial \theta} + \frac{1}{r_1 \sin\theta}\frac{\partial \overline{\sigma}_{\theta\phi}}{\partial \phi} + \frac{[\overline{\sigma}_{\theta\theta} - \overline{\sigma}_{\phi\phi}]\cos\theta}{r_1 \sin\theta} && \text{(traction equilibrium at } r = r_1) \\
& && && \quad + \sigma^{(2)}_{r\theta}(r_1) - \sigma^{(1)}_{r\theta}(r_1) = 0\,, && \\
&\sigma^{(2)}_{rr}(r_2) = \beta \sin^2\theta \cos 2\phi\,, && && \sigma^{(2)}_{r\theta}(r_2) = \beta \sin\theta \cos\theta \cos 2\phi\,, && \text{(traction at } r = r_2)
\end{aligned} \tag{30}$$

Further details regarding the construction of the system of equations are available in Appendix A.2. If the RVE is substituted by an equivalent homogeneous medium, applying the boundary condition (29) results in the displacement field

$$u^{\mathrm{eq}}_r = \frac{\beta}{2^{\mathrm{M}}\mu} r \sin^2\theta \cos 2\phi\,, \quad u^{\mathrm{eq}}_\theta = \frac{\beta}{2^{\mathrm{M}}\mu} r \sin\theta \cos\theta \cos 2\phi\,, \quad u^{\mathrm{eq}}_\phi = -\frac{\beta}{2^{\mathrm{M}}\mu} r \sin\theta \sin 2\phi\,. \tag{31}$$

Having all the displacement and stress fields, according to Eq. (16), the overall energy in both RVE and the equivalent homogeneous medium read

$$U^{\mathrm{RVE}} = \frac{\beta^2}{5}\left[5\Xi^{(2)}_1 - 7\left[1 + 3\frac{\kappa_2}{\mu_2}\right] f^{-2/3}\Xi^{(2)}_2 + 6\left[2 + \frac{\kappa_2}{\mu_2}\right] f\Xi^{(2)}_4 \right] \qquad \text{and} \qquad U^{\mathrm{eq}} = \frac{\beta^2}{2^{\mathrm{M}}\mu}\,, \tag{32}$$

resulting in a *semi-explicit* expression for the stress bound on the effective shear modulus

$$ {}^{\mathrm{M}}\mu_{\mathrm{stress}} = \frac{5}{2}\left[5\Xi_1^{(2)} - 7\left[1+3\frac{\kappa_2}{\mu_2}\right]f^{-2/3}\Xi_2^{(2)} + 6\left[2+\frac{\kappa_2}{\mu_2}\right]f\Xi_4^{(2)}\right]^{-1}, \tag{33} $$

where $\Xi_1^{(2)}$, $\Xi_2^{(2)}$ and $\Xi_4^{(2)}$ are the solutions of the system of equations (A.3).

3.2.4. Effective shear modulus

In order to obtain the effective shear modulus ${}^{\mathrm{M}}\mu$ of a particle reinforced composite, we employ the method proposed by Christensen and Lo (1979) considering an infinite effective medium surrounding the matrix whose properties are the unknowns of our problem. Consider the RVE subject to a deviatoric displacement field

$$ \boldsymbol{u}^0_{(x,y,z)} = \begin{bmatrix} \beta y \\ -\beta x \\ 0 \end{bmatrix} \quad \text{and} \quad u^0_{(r,\theta,\phi)} = \begin{bmatrix} \beta r \sin^2\theta\cos 2\phi \\ \beta r \sin\theta\cos\theta\cos 2\phi \\ -\beta r \sin\theta \sin 2\phi \end{bmatrix}. \tag{34} $$

The displacement field in the particle and the matrix for this type of boundary condition is similar to Eq. (24), see Christensen and Lo (1979) for further details. The displacement field in the effective medium reads

$$ \begin{aligned} u_r^{(\mathrm{eff})}(r,\theta,\phi) &= \beta\, r\, U_r^{(\mathrm{eff})}(r)\ \sin^2\theta\cos 2\phi\,, \\ u_\theta^{(\mathrm{eff})}(r,\theta,\phi) &= \beta\, r\, U_\theta^{(\mathrm{eff})}(r)\ \sin\theta\cos\theta\cos 2\phi\,, \\ u_\phi^{(\mathrm{eff})}(r,\theta,\phi) &= -\beta\, r\, U_\theta^{(\mathrm{eff})}(r)\ \sin\theta\sin 2\phi\,, \end{aligned} \quad \text{with} \quad \begin{cases} U_r^{(\mathrm{eff})}(r) = 1 + \dfrac{3\Xi_3^{(\mathrm{eff})}}{[r/r_1]^5} + \left[3+3\dfrac{{}^{\mathrm{M}}\kappa}{{}^{\mathrm{M}}\mu}\right]\dfrac{\Xi_4^{(\mathrm{eff})}}{[r/r_1]^3}\,, \\ U_\theta^{(\mathrm{eff})}(r) = 1 - \dfrac{2\Xi_3^{(\mathrm{eff})}}{[r/r_1]^5} + \dfrac{2\Xi_4^{(\mathrm{eff})}}{[r/r_1]^3}\,. \end{cases} \tag{35} $$

Perfect bonding between the effective medium and the matrix is assumed which renders

$$ \begin{aligned} &u_r^{(2)}(r_2,\theta,\phi) = u_r^{(\mathrm{eff})}(r_2,\theta,\phi)\,, \quad u_\theta^{(2)}(r_2,\theta,\phi) = u_\theta^{(\mathrm{eff})}(r_2,\theta,\phi)\,, \quad u_\phi^{(2)}(r_2,\theta,\phi) = u_\phi^{(\mathrm{eff})}(r_2,\theta,\phi)\,, \\ &\sigma_{rr}^{(2)}(r_2,\theta,\phi) = \sigma_{rr}^{(\mathrm{eff})}(r_2,\theta,\phi)\,, \quad \sigma_{r\theta}^{(2)}(r_2,\theta,\phi) = \sigma_{r\theta}^{(\mathrm{eff})}(r_2,\theta,\phi)\,, \quad \sigma_{r\phi}^{(2)}(r_2,\theta,\phi) = \sigma_{r\phi}^{(\mathrm{eff})}(r_2,\theta,\phi)\,. \end{aligned} \tag{36} $$

So far our problem contains ten unknowns of $\Xi_1^{(1)}$, $\Xi_2^{(1)}$, $\Xi_3^{(1)}$, $\Xi_4^{(1)}$, $\Xi_1^{(2)}$, $\Xi_2^{(2)}$, $\Xi_3^{(2)}$, $\Xi_4^{(2)}$, $\Xi_3^{(\mathrm{eff})}$ and $\Xi_4^{(\mathrm{eff})}$ which can be calculated using the boundary and interface conditions

$$
\begin{aligned}
&u_r^{(1)}, u_\theta^{(1)} \text{ finite at } r=0 \quad \rightarrow \quad \Xi_3^{(1)} = \Xi_4^{(1)} = 0\,, && \text{(finite displacement at } r=0)\\
&\bar{t}_r = \bar{k}_r \llbracket u_r \rrbracket \quad \rightarrow \quad \sigma_{rr}^{(2)}(r_1) + \sigma_{rr}^{(1)}(r_1) = 2\bar{k}_r \left[u_r^{(2)}(r_1) - u_r^{(1)}(r_1)\right], && \text{(traction average at } r=r_1)\\
&\bar{t}_\theta = \bar{k}_\theta \llbracket u_\theta \rrbracket \quad \rightarrow \quad \sigma_{r\theta}^{(2)}(r_1) + \sigma_{r\theta}^{(1)}(r_1) = 2\bar{k}_\theta \left[u_\theta^{(2)}(r_1) - u_\theta^{(1)}(r_1)\right], && \text{(traction average at } r=r_1)\\
&\left[\overline{\operatorname{div}\sigma}\right]_r + \llbracket t_r \rrbracket = 0 \quad \rightarrow \quad -\frac{\overline{\sigma}_{\theta\theta} + \overline{\sigma}_{\phi\phi}}{r_1} + \sigma_{rr}^{(2)}(r_1) - \sigma_{rr}^{(1)}(r_1) = 0\,, && \text{(traction equilibrium at } r=r_1)\\
&\left[\overline{\operatorname{div}\sigma}\right]_\theta + \llbracket t_\theta \rrbracket = 0 \quad \rightarrow \quad \frac{1}{r_1}\frac{\partial \overline{\sigma}_{\theta\theta}}{\partial\theta} + \frac{1}{r_1\sin\theta}\frac{\partial \overline{\sigma}_{\theta\phi}}{\partial\phi} + \frac{[\overline{\sigma}_{\theta\theta} - \overline{\sigma}_{\phi\phi}]\cos\theta}{r_1\sin\theta} && \text{(traction equilibrium at } r=r_1)\\
&\qquad\qquad + \sigma_{r\theta}^{(2)}(r_1) - \sigma_{r\theta}^{(1)}(r_1) = 0\,,\\
&\sigma_{rr}^{(2)}(r_2) = \sigma_{rr}^{(\mathrm{eff})}(r_2)\,, \qquad \sigma_{r\theta}^{(2)}(r_2) = \sigma_{r\theta}^{(\mathrm{eff})}(r_2)\,, && \text{(traction equilibrium at } r=r_1)\\
&u_r^{(2)}(r_2) = u_r^{(\mathrm{eff})}(r_2)\,, \qquad u_\theta^{(2)}(r_2) = u_\theta^{(\mathrm{eff})}(r_2)\,. && \text{(displacement continuity at } r=r_2)
\end{aligned}
\tag{37}
$$

Further details regarding the construction of the system of equations are available in Appendix A.3. Considering a homogeneous equivalent medium under the same boundary condition, the displacement field in the medium is similar to Eq. (26). From the Eshelby's energy principle, we can deduce

$$
\int_0^{2\pi}\int_0^{\pi} [\sigma_{rr}^{(\mathrm{eff})} u_r^{\mathrm{eq}} + \sigma_{r\theta}^{(\mathrm{eff})} u_\theta^{\mathrm{eq}} + \sigma_{r\phi}^{(\mathrm{eff})} u_\phi^{\mathrm{eq}} - \sigma_{rr}^{\mathrm{eq}} u_r^{(\mathrm{eff})} - \sigma_{r\theta}^{\mathrm{eq}} u_\theta^{(\mathrm{eff})} - \sigma_{r\phi}^{\mathrm{eq}} u_\phi^{(\mathrm{eff})}]_{r=r_2} \sin\theta \,\mathrm{d}\theta\,\mathrm{d}\phi = 0\,. \tag{38}
$$

Substituting the stress and displacement fields of the RVE and equivalent homogeneous medium at $r=r_2$ in this integral results in $\Xi_4^{(\mathrm{eff})}=0$. Unlike the macroscopic bulk modulus ${}^{\mathrm{M}}\kappa$, it is not possible to provide an explicit expression for the effective shear modulus ${}^{\mathrm{M}}\mu$ and identify its simplified forms for various interface types. Nonetheless, we have developed the following *semi-explicit* expression to obtain the macroscopic shear modulus ${}^{\mathrm{M}}\mu$

$$
{}^{\mathrm{M}}\mu = \frac{1}{80}\left[b_6 - b_5 + 12a_6 + 8a_5 + \sqrt{\Delta}\right] \quad \text{with} \quad \Delta = \left[b_6 - b_5 + 12a_6 + 8a_5\right]^2 - 80\left[a_5 b_6 - b_5 a_6\right], \tag{39}
$$

where the constants a_5, a_6, b_5 and b_6 are obtained from the solution of the system of equations (A.5) and using Eqs.(A.8) and (A.10), see Appendix A.3.

3.3. Generalized interface-enhanced Mori-Tanaka approach

In this section we elaborate our second methodology which furnishes the global interaction (dilute concentration) tensors for the of system inhomogeneity+interface in a particulate composite. The idea of providing interaction

tensors is motivated by similar techniques in the literature for coated particles or fibers (Benveniste et al., 1989; Wang et al., 2018, 2016a,b). Our proposed method is similar to (Duan et al., 2007; Gu et al., 2014), but instead of looking for an equivalent particle, we seek global strain and stress tensors of the inhomogeneity/interface system. Therefore, not only can we determine the overall properties of a composite but also we will be able to determine the state of the stress and strain in each phase of the medium including the interface. This provides a significant insight towards understanding of the behavior of composites.

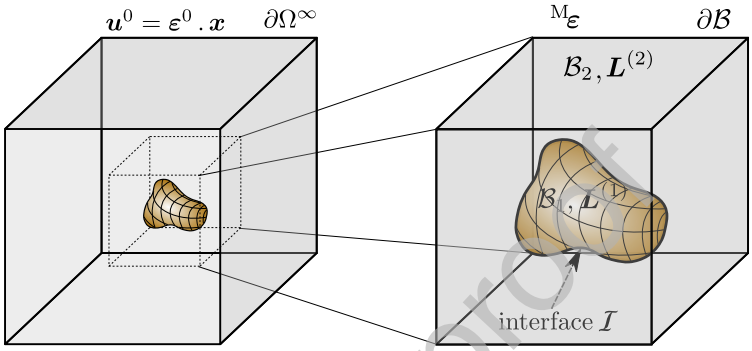

Figure 5: Inhomogeneity with imperfect interface inside an infinite matrix (left) and the RVE consisting of the inhomogeneity with imperfect interface inside a matrix material (right).

In Fig. 5 (left), the inhomogeneity with the elasticity modulus $\boldsymbol{L}^{(1)}$ occupies the space Ω_1 surrounded by the imperfect interface $\mathcal{I}$ and is embedded in an infinite matrix with the elasticity tensor $\boldsymbol{L}^{(2)}$. The matrix occupies the space Ω_2 and is subject to a linear displacement $\boldsymbol{u}^0 = \boldsymbol{\varepsilon}^0 \,.\, \boldsymbol{x}$ at far field $\partial\Omega^\infty$, see Chatzigeorgiou et al. (2017) for further details. Gu et al. (2014), based on the methodology developed by Duan et al. (2007), proposed to substitute the inhomogeneity+interface system with an equivalent particle, using energy principles. Instead of that methodology, here we propose to determine the dilute strain concentration tensor and dilute stress-strain concentration tensor for the same system according to the relations

$$\langle\boldsymbol{\varepsilon}\rangle^+_{\Omega_1} = \boldsymbol{T} : \boldsymbol{\varepsilon}^0 = \frac{1}{2|\Omega_1|}\int_{\mathcal{I}} [\boldsymbol{u}^+ \otimes \overline{\boldsymbol{n}} + \overline{\boldsymbol{n}} \otimes \boldsymbol{u}^+]\,\mathrm{d}A \qquad \text{and} \qquad \langle\boldsymbol{\sigma}\rangle^+_{\Omega_1} = \boldsymbol{H} : \boldsymbol{\varepsilon}^0 = \frac{1}{|\Omega_1|}\int_{\Omega_1} \boldsymbol{\sigma}^-\,\mathrm{d}V + \frac{1}{|\Omega_1|}\int_{\mathcal{I}} \overline{\sigma}\,\mathrm{d}A\,. \quad (40)$$

Also, one can identify the pure particle concentration tensor as

$$\langle\boldsymbol{\varepsilon}\rangle^-_{\Omega_1} = \boldsymbol{T}^{(1)} : \boldsymbol{\varepsilon}^0 = \frac{1}{2|\Omega_1|}\int_{\mathcal{I}} [\boldsymbol{u}^- \otimes \overline{\boldsymbol{n}} + \overline{\boldsymbol{n}} \otimes \boldsymbol{u}^-]\,\mathrm{d}A\,. \quad (41)$$

Now, consider an RVE that occupies the space $\mathcal{B}$ with the boundary $\partial\mathcal{B}$ and the volume $\mathcal{V}$ subject to macroscopic strain ${}^{\mathrm{M}}\boldsymbol{\varepsilon}$ as shown in Fig. 5 (right). The inhomogeneity occupies the space $\mathcal{B}_1$ with volume $\mathcal{V}_1$ and the matrix occupies the space $\mathcal{B}_2$ with volume $\mathcal{V}_2$. Obviously, we have $\mathcal{B} = \mathcal{B}_1 \cup \mathcal{B}_2$ and $\mathcal{V} = \mathcal{V}_1 + \mathcal{V}_2$ and the inhomogeneity volume

fraction reads $f = \mathscr{V}_1/\mathscr{V}$. The macroscopic strain and stress tensors are related to the corresponding fields in the inhomogeneity and the interface according to

$$\begin{aligned} {}^{\mathrm{M}}\boldsymbol{\varepsilon} &= \frac{1}{\mathscr{V}}\int_{\mathcal{B}} \boldsymbol{\varepsilon}\,\mathrm{d}V + \frac{1}{2\mathscr{V}}\int_{I} \left[\llbracket \boldsymbol{u} \rrbracket \otimes \overline{\boldsymbol{n}} + \overline{\boldsymbol{n}} \otimes \llbracket \boldsymbol{u} \rrbracket\right] \mathrm{d}A = [1-f]\boldsymbol{\varepsilon}^{(2)} + f\boldsymbol{\varepsilon}^{(1)} + \widehat{\boldsymbol{\varepsilon}}\,, \\ {}^{\mathrm{M}}\boldsymbol{\sigma} &= \frac{1}{\mathscr{V}}\int_{\mathcal{B}} \boldsymbol{\sigma}\,\mathrm{d}V + \frac{1}{\mathscr{V}}\int_{I} \overline{\sigma}\,\mathrm{d}A = [1-f]\boldsymbol{L}^{(2)} : \boldsymbol{\varepsilon}^{(2)} + f\boldsymbol{L}^{(1)} : \boldsymbol{\varepsilon}^{(1)} + \widehat{\boldsymbol{\sigma}}\,, \end{aligned} \tag{42}$$

where

$$\boldsymbol{\varepsilon}^{(1)} = \frac{1}{\mathscr{V}_1}\int_{\mathcal{B}_1} \boldsymbol{\varepsilon}\,\mathrm{d}V\,, \qquad \boldsymbol{\varepsilon}^{(2)} = \frac{1}{\mathscr{V}_2}\int_{\mathcal{B}_2} \boldsymbol{\varepsilon}\,\mathrm{d}V \qquad \text{and} \qquad \widehat{\boldsymbol{\varepsilon}} = \frac{1}{2\mathscr{V}}\int_{I} \left[\llbracket \boldsymbol{u} \rrbracket \otimes \overline{\boldsymbol{n}} + \overline{\boldsymbol{n}} \otimes \llbracket \boldsymbol{u} \rrbracket\right] \mathrm{d}A\,, \tag{43}$$

are the average strains of the matrix, inhomogeneity and interface, respectively. The average stress on the interface reads

$$\widehat{\boldsymbol{\sigma}} = \frac{1}{\mathscr{V}}\int_{I} \overline{\boldsymbol{\sigma}}\,\mathrm{d}A\,. \tag{44}$$

Utilizing the interaction tensors (40) and (41), the interface-enhanced Mori–Tanaka scheme results in

$$\boldsymbol{\varepsilon}^{(1)} = \boldsymbol{T}^{(1)} : \boldsymbol{\varepsilon}^{(2)}\,, \qquad \boldsymbol{\varepsilon}^{(1)} + \frac{1}{f}\widehat{\boldsymbol{\varepsilon}} = \boldsymbol{T} : \boldsymbol{\varepsilon}^{(2)}\,, \qquad \boldsymbol{L}^{(1)} : \boldsymbol{\varepsilon}^{(1)} + \frac{1}{f}\widehat{\boldsymbol{\sigma}} = \boldsymbol{H} : \boldsymbol{\varepsilon}^{(2)}\,. \tag{45}$$

Thus, Eq. $(42)_1$ yields

$${}^{\mathrm{M}}\boldsymbol{\varepsilon} = \left[[1-f]\mathbb{I} + f\boldsymbol{T}\right]\boldsymbol{\varepsilon}^{(2)} \qquad \text{or} \qquad \boldsymbol{\varepsilon}^{(2)} = \boldsymbol{A}^{(2)} : {}^{\mathrm{M}}\boldsymbol{\varepsilon}\,, \tag{46}$$

with $\mathbb{I}$ being the fourth order identity tensor and $\boldsymbol{A}^{(2)} = [[1-f]\mathbb{I} + f\boldsymbol{T}]^{-1}$. On the other hand, Eq. $(42)_2$ yields

$${}^{\mathrm{M}}\boldsymbol{\sigma} = \left[[1-f]\boldsymbol{L}^{(2)} + f\boldsymbol{H}\right] : \boldsymbol{\varepsilon}^{(2)} = \left[[1-f]\boldsymbol{L}^{(2)} + f\boldsymbol{H}\right] : \boldsymbol{A}^{(2)} : {}^{\mathrm{M}}\boldsymbol{\varepsilon}\,. \tag{47}$$

Accordingly, the macroscopic stiffness tensor reads

$${}^{\mathrm{M}}\boldsymbol{L} = \left[[1-f]\boldsymbol{L}^{(2)} + f\boldsymbol{H}\right] : \boldsymbol{A}^{(2)}, \tag{48}$$

and the properties of the equivalent particle in (Gu et al., 2014) can be recovered according to $\boldsymbol{L}^{\mathrm{eq}} = \boldsymbol{H} : \boldsymbol{T}^{-1}$. For a

given macroscopic strain ${}^{\mathrm{M}}\boldsymbol{\varepsilon}$, the average stress and strain in the particle and the matrix are

$$\begin{aligned} \boldsymbol{\sigma}^{(1)} &= \boldsymbol{L}^{(1)} : \boldsymbol{\varepsilon}^{(1)} = \boldsymbol{L}^{(1)} : \boldsymbol{T}^{(1)} : \boldsymbol{A}^{(2)} : {}^{\mathrm{M}}\boldsymbol{\varepsilon}\,, \qquad & \boldsymbol{\varepsilon}^{(1)} &= \boldsymbol{T}^{(1)} : \boldsymbol{A}^{(2)} : {}^{\mathrm{M}}\boldsymbol{\varepsilon}\,, \\ \boldsymbol{\sigma}^{(2)} &= \boldsymbol{L}^{(2)} : \boldsymbol{\varepsilon}^{(2)} = \boldsymbol{L}^{(2)} : \boldsymbol{A}^{(2)} : {}^{\mathrm{M}}\boldsymbol{\varepsilon}\,, & \boldsymbol{\varepsilon}^{(2)} &= \boldsymbol{A}^{(2)} : {}^{\mathrm{M}}\boldsymbol{\varepsilon}\,. \end{aligned} \tag{49}$$

Exploiting Eq. (45), the average stress and strain on the interface are given by

$$\widehat{\boldsymbol{\sigma}} = f\left[\boldsymbol{H} - \boldsymbol{L}^{(1)} : \boldsymbol{T}^{(1)}\right] : \boldsymbol{A}^{(2)} : {}^{\mathrm{M}}\boldsymbol{\varepsilon} \qquad \text{and} \qquad \widehat{\boldsymbol{\varepsilon}} = f\left[\boldsymbol{T} - \boldsymbol{T}^{(1)}\right] : \boldsymbol{A}^{(2)} : {}^{\mathrm{M}}\boldsymbol{\varepsilon}\,. \tag{50}$$

In order to complete the homogenization framework, we must determine the interaction tensors $\boldsymbol{H}$, $\boldsymbol{T}$ and $\boldsymbol{T}^{(1)}$. In doing so, we employ the Eshelby's inhomogeneity problem for *isochoric* and *deviatoric* conditions. For a particle reinforced composite with isotropic constituents, the interaction tensors are isotropic and can be written as

$$\boldsymbol{T}^{(1)} = 3T^{b(1)}\boldsymbol{\mathcal{I}}^{h} + 2T^{s(1)}\boldsymbol{\mathcal{I}}^{d}\,, \quad \boldsymbol{T} = 3T^{b}\boldsymbol{\mathcal{I}}^{h} + 2T^{s}\boldsymbol{\mathcal{I}}^{d}\,, \quad \boldsymbol{H} = 3H^{b}\boldsymbol{\mathcal{I}}^{h} + 2H^{s}\boldsymbol{\mathcal{I}}^{d} \quad \text{with} \quad \boldsymbol{\mathcal{I}}^{h} = \frac{1}{3}\boldsymbol{i}\otimes\boldsymbol{i}\,, \quad \boldsymbol{\mathcal{I}}^{d} = \boldsymbol{\mathcal{I}} - \boldsymbol{\mathcal{I}}^{h}\,. \tag{51}$$

3.3.1. Isochoric conditions

Assume an RVE consisting of an infinite matrix with a spherical inhomogeneity subject to a hydrostatic far field displacement according to

$$\boldsymbol{u}^{0}_{(x,y,z)} = \begin{bmatrix} \beta x \\ \beta y \\ \beta z \end{bmatrix} \quad \text{and} \quad \boldsymbol{u}^{0}_{(r,\theta,\phi)} = \begin{bmatrix} \beta r \\ 0 \\ 0 \end{bmatrix}. \tag{52}$$

For this boundary condition, the displacement fields in the matrix and fiber are similar to Eq. (18) with the unknowns $\Xi_1^{(1)}$, $\Xi_2^{(1)}$, $\Xi_1^{(2)}$ and $\Xi_2^{(2)}$. The boundary and interface conditions lead to the following equations

$$\begin{aligned} & u_r^{(1)} \text{ finite at } r = 0 && \rightarrow && \Xi_2^{(1)} = 0\,, && \text{(finite displacement at } r = 0) \\ & \bar{t}_r = \bar{k}_r \left[\!\left[u_r\right]\!\right] && \rightarrow && \frac{\sigma_{rr}^{(2)}(r_1) + \sigma_{rr}^{(1)}(r_1)}{2} = \bar{k}_r\left[u_r^{(2)}(r_1) - u_r^{(1)}(r_1)\right], && \text{(traction average at } r = r_1) \\ & \left[\overline{\operatorname{div}}\,\overline{\sigma}\right]_r + \left[\!\left[t_r\right]\!\right] = 0 && \rightarrow && -\frac{\overline{\sigma}_{\theta\theta} + \overline{\sigma}_{\phi\phi}}{r_1} + \sigma_{rr}^{(2)}(r_1) - \sigma_{rr}^{(1)}(r_1) = 0\,, && \text{(traction equilibrium at } r = r_1) \\ & u_r^{(2)}(r \rightarrow \infty) = \beta r\,, && \rightarrow && \Xi_1^{(2)} = 1\,, && \text{(displacement at } r \rightarrow \infty) \end{aligned} \tag{53}$$

resulting in the linear system of equations

$$\begin{bmatrix} 1+\dfrac{3\kappa_1}{2\bar{k}r_1} & -1-\dfrac{2\mu_2}{\bar{k}r_1} \\ 3\kappa_1+\dfrac{2\bar{k}}{r_1} & 4\mu_2+\dfrac{2\left[\bar{\lambda}+\bar{\mu}\right]}{r_1} \end{bmatrix} \begin{bmatrix} \Xi_1^{(1)} \\ \Xi_2^{(2)} \end{bmatrix} = \begin{bmatrix} 1-\dfrac{3\kappa_2}{2\bar{k}r_1} \\ 3\kappa_2-\dfrac{2\left[\bar{\lambda}+\bar{\mu}\right]}{r_1} \end{bmatrix}. \tag{54}$$

Solving this system, the average strain in the particle and the strain and stress fields in the particle+interface system are obtained as

$$\int_{\mathcal{B}} \boldsymbol{\varepsilon}^{-}_{\Omega_1}\,\mathrm{d}V = \Xi_1^{(1)}\,\boldsymbol{\varepsilon}^0\,, \qquad \int_{\mathcal{B}} \boldsymbol{\varepsilon}^{+}_{\Omega_1}\,\mathrm{d}V = \left[1+\Xi_2^{(2)}\right]\boldsymbol{\varepsilon}^0\,, \qquad \int_{\mathcal{B}} \boldsymbol{\sigma}^{+}_{\Omega_1}\,\mathrm{d}V = \left[3\kappa_2-4\mu_2\Xi_2^{(2)}\right]\boldsymbol{\varepsilon}^0\,. \tag{55}$$

Consequently, the bulk interaction terms read

$$3T^{b(1)} = \Xi_1^{(1)}\,, \qquad 3T^{b} = 1+\Xi_2^{(2)}\,, \qquad 3H^{b} = 3\kappa_2-4\mu_2\Xi_2^{(2)}\,, \tag{56}$$

where $\Xi_1^{(1)}$ and $\Xi_2^{(2)}$ are obtained from the solution of the linear system (54).

3.3.2. Deviatoric conditions

Assume the RVE is subject to a deviatoric far field displacement

$$\boldsymbol{u}^0_{(x,y,z)} = \begin{bmatrix} \beta y \\ -\beta x \\ 0 \end{bmatrix} \quad \text{and} \quad u^0_{(r,\theta,\phi)} = \begin{bmatrix} \beta r \sin^2\theta\cos 2\phi \\ \beta r \sin\theta\cos\theta\cos 2\phi \\ -\beta r \sin\theta\sin 2\phi \end{bmatrix}. \tag{57}$$

For this boundary condition, the displacement fields in the matrix and fiber are similar to Eq. (24) with the unknowns $\Xi_1^{(1)}$, $\Xi_2^{(1)}$, $\Xi_3^{(1)}$, $\Xi_4^{(1)}$, $\Xi_1^{(2)}$, $\Xi_2^{(2)}$, $\Xi_3^{(2)}$ and $\Xi_4^{(2)}$. The boundary and interface conditions lead to the following equations

$$
\begin{aligned}
&u_r^{(1)}, u_\theta^{(1)} \text{ finite at } r = 0 && \rightarrow \quad \Xi_3^{(1)} = \Xi_4^{(1)} = 0\,, && \text{finite displacement at } r = 0\\
&\bar{t}_r = \overline{k}_r \left[\!\left[u_r\right]\!\right] && \rightarrow \quad \sigma_{rr}^{(2)}(r_1) + \sigma_{rr}^{(1)}(r_1) = 2\overline{k}_r \left[u_r^{(2)}(r_1) - u_r^{(1)}(r_1)\right], && \text{(traction average at } r = r_1)\\
&\bar{t}_\theta = \overline{k}_\theta \left[\!\left[u_\theta\right]\!\right] && \rightarrow \quad \sigma_{r\theta}^{(2)}(r_1) + \sigma_{r\theta}^{(1)}(r_1) = 2\overline{k}_\theta \left[u_\theta^{(2)}(r_1) - u_\theta^{(1)}(r_1)\right], && \text{(traction average at } r = r_1)\\
&\left[\overline{\operatorname{div}\overline{\sigma}}\right]_r + \left[\!\left[t_r\right]\!\right] = 0 && \rightarrow \quad -\frac{\overline{\sigma}_{\theta\theta} + \overline{\sigma}_{\phi\phi}}{r_1} + \sigma_{rr}^{(2)}(r_1) - \sigma_{rr}^{(1)}(r_1) = 0\,, && \text{(traction equilibrium at } r = r_1)\\
&\left[\overline{\operatorname{div}\overline{\sigma}}\right]_\theta + \left[\!\left[t_\theta\right]\!\right] = 0 && \rightarrow \quad \frac{1}{r_1}\frac{\partial\overline{\sigma}_{\theta\theta}}{\partial\theta} + \frac{1}{r_1\sin\theta}\frac{\partial\overline{\sigma}_{\theta\phi}}{\partial\phi} + \frac{[\overline{\sigma}_{\theta\theta} - \overline{\sigma}_{\phi\phi}]\cos\theta}{r_1\sin\theta} && \text{(traction equilibrium at } r = r_1)\\
& && \qquad + \sigma_{r\theta}^{(2)}(r_1) - \sigma_{r\theta}^{(1)}(r_1) = 0\,, &&\\
&u_r^{(2)}(r = r_2) = \beta r \sin^2\theta\cos 2\phi && \rightarrow \quad \Xi_1^{(2)} = 1\,, \quad \Xi_2^{(2)} = 0\,, && \text{(displacement at } r \to \infty)\\
&u_\theta^{(2)}(r = r_2) = \beta r \sin\theta\cos\theta\cos 2\phi && \rightarrow \quad \Xi_1^{(2)} = 1\,, \quad \Xi_2^{(2)} = 0\,, && \text{(displacement at } r \to \infty)
\end{aligned}
\tag{58}
$$

resulting in the system of equations

$$
\begin{bmatrix}
1 + \dfrac{\mu_1}{\overline{k}r_1} & 2 - 3\dfrac{\kappa_1}{\mu_1} + \zeta_1 & -3 - \dfrac{12\mu_2}{\overline{k}r_1} & -3 - 3\dfrac{\kappa_2}{\mu_2} + \zeta_2\\
1 + \dfrac{\mu_1}{\overline{k}r_1} & -\dfrac{11}{3} - 5\dfrac{\kappa_1}{\mu_1} + \zeta_3 & 2 + \dfrac{8\mu_2}{\overline{k}r_1} & -2 + \dfrac{3\kappa_2}{\overline{k}r_1}\\
2\mu_1 - \dfrac{\left[\overline{\lambda} + \overline{\mu}\right]}{r_1} & 3\kappa_1 - 2\mu_1 + \zeta_4 & 24\mu_2 + \dfrac{12\left[\overline{\lambda} + \overline{\mu}\right]}{r_1} & 18\kappa_2 + 8\mu_2 + \dfrac{6\kappa_2\left[\overline{\lambda} + \overline{\mu}\right]}{\mu_2 r_1}\\
2\mu_1 + \zeta_5 & -16\kappa_1 - \dfrac{10}{3}\mu_1 + \zeta_6 & -16\mu_2 + \zeta_7 & -6\kappa_2 + \zeta_8
\end{bmatrix}
\begin{bmatrix}
\Xi_1^{(1)}\\ \Xi_2^{(1)}\\ \Xi_3^{(2)}\\ \Xi_4^{(2)}
\end{bmatrix}
=
\begin{bmatrix}
1 - \dfrac{\mu_2}{\overline{k}r_1}\\
1 - \dfrac{\mu_2}{\overline{k}r_1}\\
2\mu_2 + \dfrac{\left[\overline{\lambda} + \overline{\mu}\right]}{r_1}\\
2\mu_2 - \zeta_5
\end{bmatrix},
\tag{59}
$$

with

$$
\begin{aligned}
&\zeta_1 = \frac{3\kappa_1 - 2\mu_1}{2\overline{k}r_1}\,, \quad \zeta_2 = -\frac{9\kappa_2 + 4\mu_2}{\overline{k}r_1}\,, \quad \zeta_3 = -\frac{24\kappa_1 + 5\mu_1}{3\overline{k}r_1}\,, \quad \zeta_4 = \frac{[9\kappa_1 + 15\mu_1]\left[\overline{\lambda} + \overline{\mu}\right]}{\mu_1 r_1}\,, \quad \zeta_5 = \frac{\left[\overline{\lambda} + 3\overline{\mu}\right]}{r_1}\,,\\
&\zeta_6 = -\frac{\kappa_1\left[9\overline{\lambda} + 19\overline{\mu}\right]}{\mu_1 r_1} - \frac{\left[45\overline{\lambda} + 67\overline{\mu}\right]}{3r_1}\,, \quad \zeta_7 = -\frac{4\left[3\overline{\lambda} + 4\overline{\mu}\right]}{r_1}\,, \quad \zeta_8 = \frac{-6\kappa_2\left[\overline{\lambda} + \overline{\mu}\right] + 4\mu_2\overline{\mu}}{\mu_2 r_1}\,.
\end{aligned}
\tag{60}
$$

Solving this system, the average strain in the particle and the strain and stress in the particle+interface system are determined as

$$\begin{aligned}
\int_{\mathcal{B}} \boldsymbol{\varepsilon}^{-}_{\Omega_1}\,\mathrm{d}V &= \frac{1}{5}\left[5\Xi_1^{(1)} - 7\left[1+3\frac{\kappa_1}{\mu_1}\right]\Xi_2^{(1)}\right]\boldsymbol{\varepsilon}^0\,,\\
\int_{\mathcal{B}} \boldsymbol{\varepsilon}^{+}_{\Omega_1}\,\mathrm{d}V &= \frac{1}{5}\left[5+6\left[2+\frac{\kappa_2}{\mu_2}\right]\Xi_4^{(2)}\right]\boldsymbol{\varepsilon}^0\,,\\
\int_{\mathcal{B}} \boldsymbol{\sigma}^{+}_{\Omega_1}\,\mathrm{d}V &= \frac{1}{5}\left[10\mu_2 - 2\left[9\kappa_2+8\mu_2\right]\Xi_4^{(2)}\right]\boldsymbol{\varepsilon}^0\,.
\end{aligned} \tag{61}$$

Consequently, the shear interaction terms read

$$2T^{s(1)} = \frac{1}{5}\left[5\Xi_1^{(1)} - 7\left[1+3\frac{\kappa_1}{\mu_1}\right]\Xi_2^{(1)}\right], \quad 2T^{s} = \frac{1}{5}\left[5+6\left[2+\frac{\kappa_2}{\mu_2}\right]\Xi_4^{(2)}\right], \quad 2H^{s} = \frac{1}{5}\left[10\mu_2 - 2\left[9\kappa_2+8\mu_2\right]\Xi_4^{(2)}\right]. \tag{62}$$

where $\Xi_1^{(1)}$, $\Xi_2^{(1)}$ and $\Xi_4^{(2)}$ are obtained from the linear system (59).

Remark The composite spheres assemblage methodology has been designed for uniform distribution of inclusions and is not extensible to more complex cases. On the other hand, the Mori–Tanaka approach is more flexible and non-uniform distributions of inclusions can be adopted by proper modification of the relations (40) and (41), see for instance (Entchev and Lagoudas, 2002). The relation between the tensors $\boldsymbol{T}$ and $\boldsymbol{A}$ provides implicitly the interactions between inclusions of different type or distribution.

4. Numerical examples

In this section, through a set of numerical examples, the accuracy of the analytical solutions are evaluated via comparison with the computational results using the finite element method. In doing so, the overall material response of particulate composites embedding general interfaces is investigated in various scenarios. It shall be emphasized that the results obtained by the computational analysis are regarded as the "exact" solution and the analytical solutions are interpreted as "approximations". The RVE in our computational study is spherical suitable for comparison with the analytical solutions. The computational analysis is carried out using our in-house finite element code applied to the RVE discretized by quadratic Lagrange elements as depicted in Fig. 6. The discretized RVE consists of overall 19208 elements and 160863 nodes. For all the examples, the solution procedures are robust and render asymptotically quadratic rate of convergence associated with the Newton–Raphson scheme. Throughout the examples, the inclusion volume fraction is assumed to be 30%. To cover a broad range of material properties, three different stiffness ratios of 0.1, 1 and 10 are examined. The stiffness ratio denoted as incl./matr. is the ratio of the inclusion Lamé parameters to the matrix Lamé parameters. The stiffness ratio 0.1 indicates a 10 times more compliant inclusion compared to

the matrix whereas the stiffness ratio 10 corresponds to a 10 times stiffer inclusion than the matrix. The stiffness ratio 1 represents identical inclusion and matrix. Obviously, the limit case of incl./matr. $\to \infty$ indicates a rigid inclusion whereas incl./matr. $= 0$ corresponds to porous media. In this study, we set the matrix material parameters to $\lambda_1 = \mu_1 = 1$ and the inclusion material parameters vary in accordance with the predefined stiffness ratios. In order to highlight the role of the general interface in the overall material response, two values of $\overline{\lambda} = \overline{\mu} = 1$ and $\overline{\lambda} = \overline{\mu} = 100$ are considered for the general interface in-plane parameters indicating a low and a high elastic resistance against in-plane stretches, respectively. On the other hand, the two considered values for the general interface orthogonal resistance against opening are $\overline{k} = 1$ indicating a low stiffness and $\overline{k} = 100$ indicating a high orthogonal resistance. In the limit of $\overline{k} = 0$, the interface shows no opening resistance resembling a totally detached matrix and particle. In contrast, the limit of $\overline{k} \to \infty$ corresponds to a coherent interface. We emphasize that our developed general interface model is capable to recover any of the cohesive, elastic or perfect interface models, see Fig. 1. The elastic interface model is recovered when $\overline{\lambda} \neq 0, \overline{\mu} \neq 0$ and $\overline{k} \to \infty$. The conditions $\overline{\lambda} = 0$ and $\overline{\mu} = 0$ recover the cohesive interface model with coherent coefficient $\overline{k}$. Finally, the perfect interface model can be considered as the coincidence of the cohesive and the elastic interface models with $\overline{\lambda} = 0, \overline{\mu} = 0$ and $\overline{k} \to \infty$.

Figures 7–9 show the effective bulk and shear moduli ${}^{\mathrm{M}}\kappa$ and ${}^{\mathrm{M}}\mu$ versus size for different stiffness ratios. Each row corresponds to a specific interface orthogonal resistance and each column corresponds to a specific interface in-plane resistance. Clearly, the first column represents the cohesive interface model due to the vanishing interface in-plane resistance. The dashed lines show the solutions obtained from the analytical approaches developed in Sections 3.2 and 3.3. The solid straight line shows the response associated with the perfect interface model. The red circular points

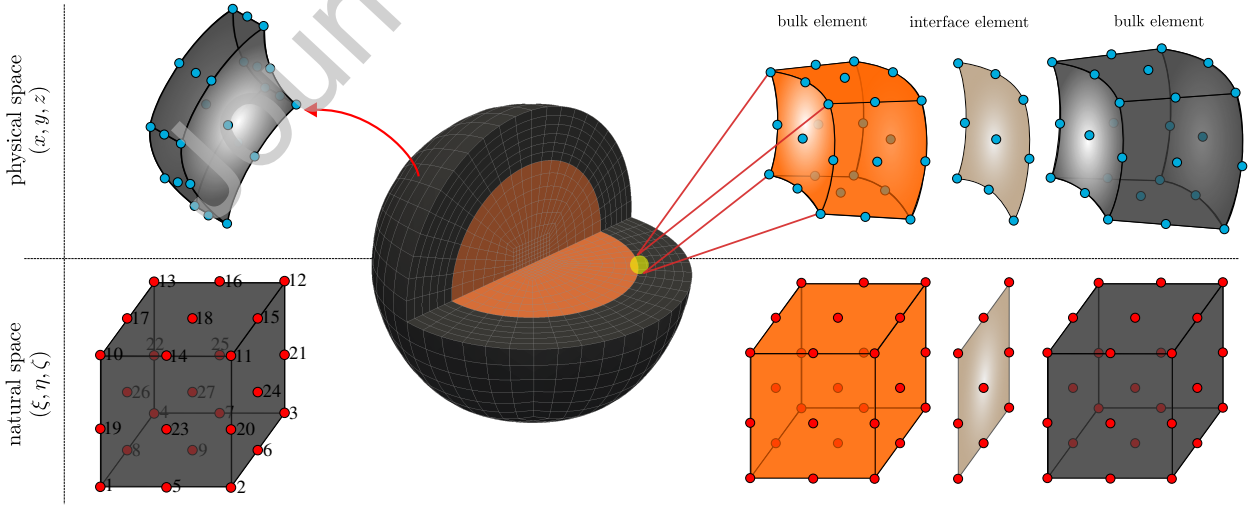

Figure 6: Discretized RVE for the FEM analysis. Quadratic Lagrange elements are employed for the FEM analysis. The elements are illustrated in both physical and natural spaces.

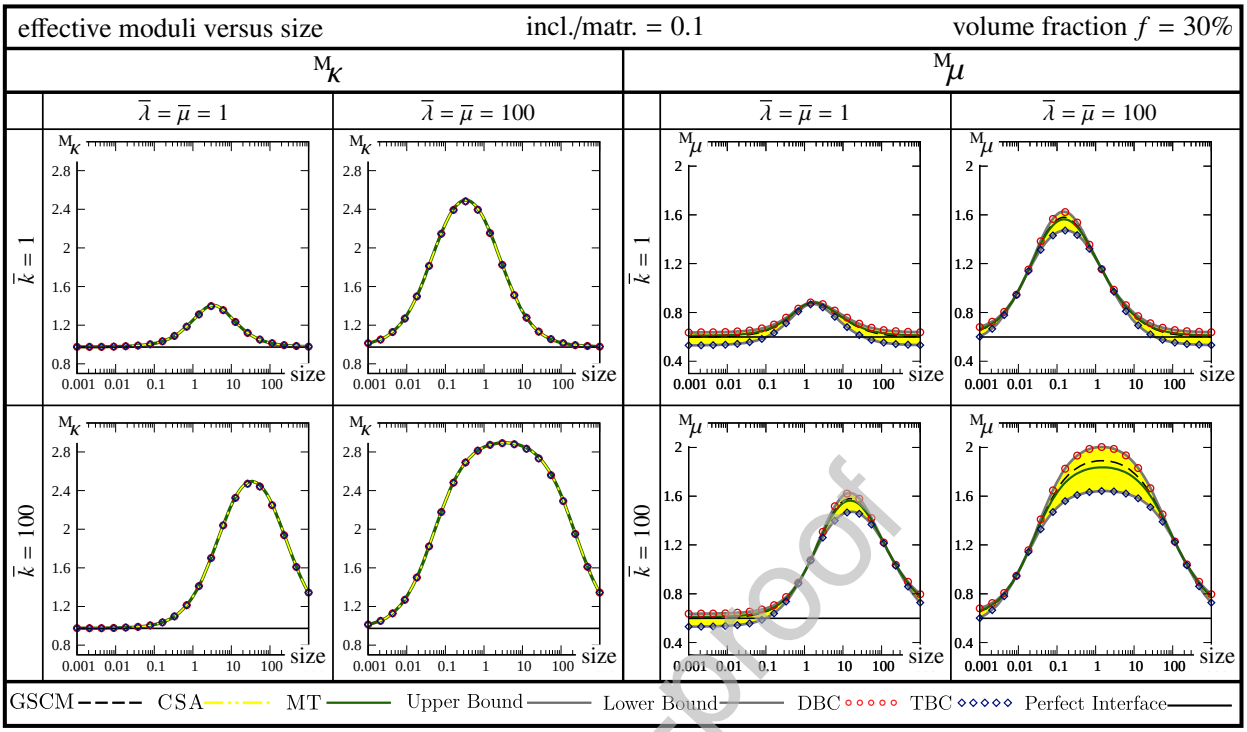

Figure 7: The macroscopic bulk and shear modulus versus size for incl./matr. = 0.1. The lines represent the analytical solutions and the dots correspond to the computational results obtained from the finite element method. "CSA" indicates the effective bulk modulus obtained via extending the composite sphere assemblage approach proposed in Section 3.2.1. "GSCM" corresponds to the effective shear modulus via extending the generalized self-consistent method proposed in Section 3.2.4. "Upper Bound" and "Lower Bound" indicate the bounds on the shear modulus addressed in Sections 3.2.2 and 3.2.3. "MT" corresponds to the extended Mori–Tanaka method developed in Section 3.3.

and blue rectangular points correspond to the computational results via imposing DBC and TBC, respectively.

A remarkable agreement is consistently obtained between the analytical and computational results. For all cases, size-dependent behavior is observed due to the presence of the interface. For the bulk modulus, all the solutions show a uniform behavior relative to the perfect interface solution. The results coincide with the perfect interface model at small sizes. As the size increases, the overall response deviates from the perfect interface solution until it reaches to an extermum at a critical size which is then followed by converging to the perfect interface solution due to negligible interface effects at large sizes. When incl./matr. = 0.1, the results from the general interface model always render a stiffer response than that of the perfect interface model. In addition, increasing any of the interface parameters stiffens the overall response. A particularly important observation is that for incl./matr. = 1, although the matrix and the inclusion are identical, various combinations of general interface parameters result in different, but yet size-dependent, overall behavior. If incl./matr. = 10, depending on the interface parameters, the general interface model could result in either stiffer or weaker response compared to the perfect interface model. Somewhat surprisingly, the overall response almost show no sensitivity to the size for some special cases, for instance, the cases with incl./matr. = 10, $\overline{\lambda} = \overline{\mu} = 1$ and $\overline{k} = 100$. For the shear modulus, there is a perfect agreement between DBC and

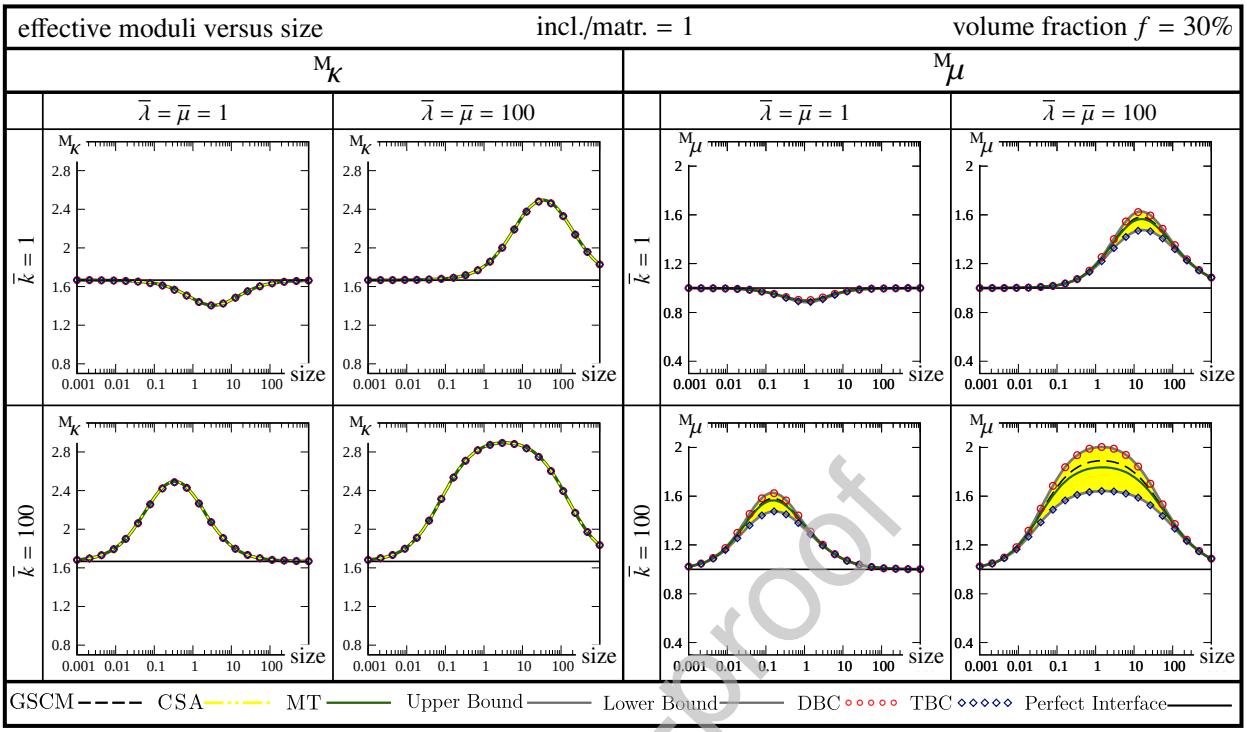

Figure 8: The macroscopic bulk and shear modulus versus size for incl./matr. = 1. The lines represent the analytical solutions and the dots correspond to the computational results obtained from the finite element method. "CSA" indicates the effective bulk modulus obtained via extending the composite sphere assemblage approach proposed in Section 3.2.1. "GSCM" corresponds to the effective shear modulus via extending the generalized self-consistent method proposed in Section 3.2.4. "Upper Bound" and "Lower Bound" indicate the bounds on the shear modulus addressed in Sections 3.2.2 and 3.2.3. "MT" corresponds to the extended Mori–Tanaka method developed in Section 3.3.

the upper bound and between TBC and the lower bound. Depending on the stiffness ratio and the general interface parameters, various observations can be drawn. For instance when incl./matr. = 0.1, the bounds coincide only at certain sizes. Increasing any of the interface parameters yields a stiffer material response. For incl./matr. = 1, there is an excellent agreement between the bounds at large sizes. This is justifiable since incl./matr. = 1 implies identical matrix and inclusion and at large sizes interface effects diminish and bulk properties play the decisive role on the overall material response. If incl./matr. = 10, the bounds agree only at few sizes for weak interfaces. Increasing any of the interface parameters widens the gap between the upper and the lower bounds. Another noteworthy observation is that the generalized self-consistent method and the modified Mori–Tanaka method do not provide similar estimates for the macroscopic shear modulus. It is observed that generally GSCM provides higher values than the MT method.

Remark In view of the behavior of the effective bulk modulus $^{M}\kappa$, it is observed that the general interface model at both limits of small and large sizes converges to the perfect interface model. The interface effect is decreasing when increasing the size and thus, its behavior at large sizes is fairly obvious. At small scales, however, further discussion is required to justify the influence of the interface on the overall material response. The effective behavior of the general interface model can be explained by the fact that it combines the two opposing cohesive and elastic interface models,

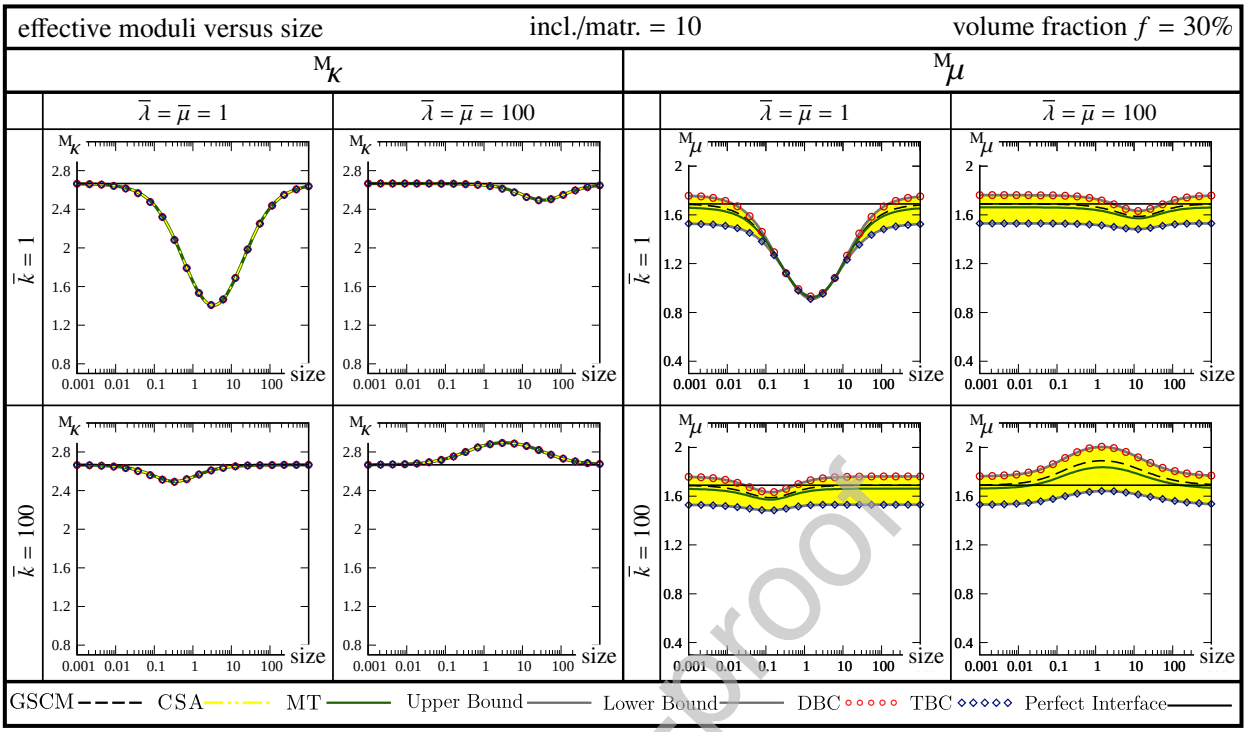

Figure 9: The macroscopic bulk and shear modulus versus size for incl./matr. = 10. The lines represent the analytical solutions and the dots correspond to the computational results obtained from the finite element method. "CSA" indicates the effective bulk modulus obtained via extending the composite sphere assemblage approach proposed in Section 3.2.1. "GSCM" corresponds to the effective shear modulus via extending the generalized self-consistent method proposed in Section 3.2.4. "Upper Bound" and "Lower Bound" indicate the bounds on the shear modulus addressed in Sections 3.2.2 and 3.2.3. "MT" corresponds to the extended Mori–Tanaka method developed in Section 3.3.

schematically illustrated in Fig. 1. The elastic interface model results in a *smaller-stronger* effect in contrast to the *smaller-weaker* effect of the cohesive interface model. At large sizes, neither of the interface effects is present. But at small sizes, both of the interface effects are present and eventually cancel each other. Furthermore, we can elaborate on this observation from an analytical perspective. To do so, we re-express the effective bulk modulus Eq. (22) as

$$ {}^{\mathrm{M}}\kappa = \frac{3\big[\overline{\lambda}+\overline{\mu}+\overline{k}r_1^2\big]\big[\kappa_2[3\kappa_1+4\mu_2]+4f\mu_2[\kappa_1-\kappa_2]\big]+4\overline{k}r_1\big[\overline{\lambda}+\overline{\mu}\big]\big[3\kappa_2+4f\mu_2\big]+36\kappa_1\kappa_2\mu_2 r_1\big[1-f\big]}{3\big[\overline{\lambda}+\overline{\mu}\big]\big[3\kappa_1+4\mu_2+3f[\kappa_2-\kappa_1]+4\overline{k}r_1[1-f]\big]+3\overline{k}r_1^2\big[3\kappa_1+4\mu_2+3f[\kappa_2-\kappa_1]\big]+9\kappa_1 r_1\big[4\mu_2+3\kappa_2\big]} $$

thereby gaining a better insight on ${}^{\mathrm{M}}\kappa$ in terms of r_1. This relation in both limits simplifies to

$$ r\to 0 \quad \text{or} \quad r\to\infty \qquad \Rightarrow \qquad {}^{\mathrm{M}}\kappa = \kappa_2 + \frac{f[\kappa_1-\kappa_2][4\mu_2+3\kappa_2]}{4\mu_2+3\kappa_1+3f[\kappa_2-\kappa_1]} \tag{63} $$

which corresponds exactly to the solution associated with the perfect interface model.

Motivated by the observations throughout the examples, we can identify two distinctive *size-dependent bounds* and *ultimate bounds*, depicted in Fig. 10. Size-dependent bounds are the bounds on the overall properties of the

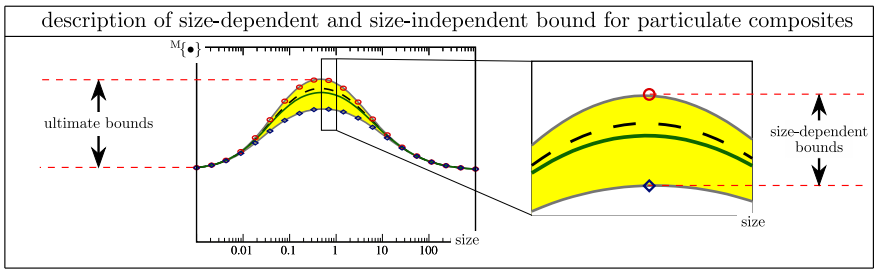

Figure 10: Illustration of size-dependent and ultimate bounds. The size-dependent bounds are the bounds on the effective behavior of the microstructure at any given size. The ultimate bounds are size independent and entirely depend on the interface and bulk material properties.

composites at any specific size. These bounds correspond to the boundary value problem solution associated with DBC providing the upper bound and TBC providing the lower bound. On the other hand, regardless of the RVE size, the macroscopic response is always bounded between two extreme values referred to as ultimate bounds. These bounds are independent of the size and they solely depend on the interface and bulk material properties. As shown in Fig. 10, one of the ultimate bounds is reached at a critical size between the limits and the other one is reached at extreme sizes whereas size-dependent bounds are local in the sense that for specific material and interface parameters, they vary as the size changes. Note that the size-dependent bounds are only distinguishable in the case of the overall

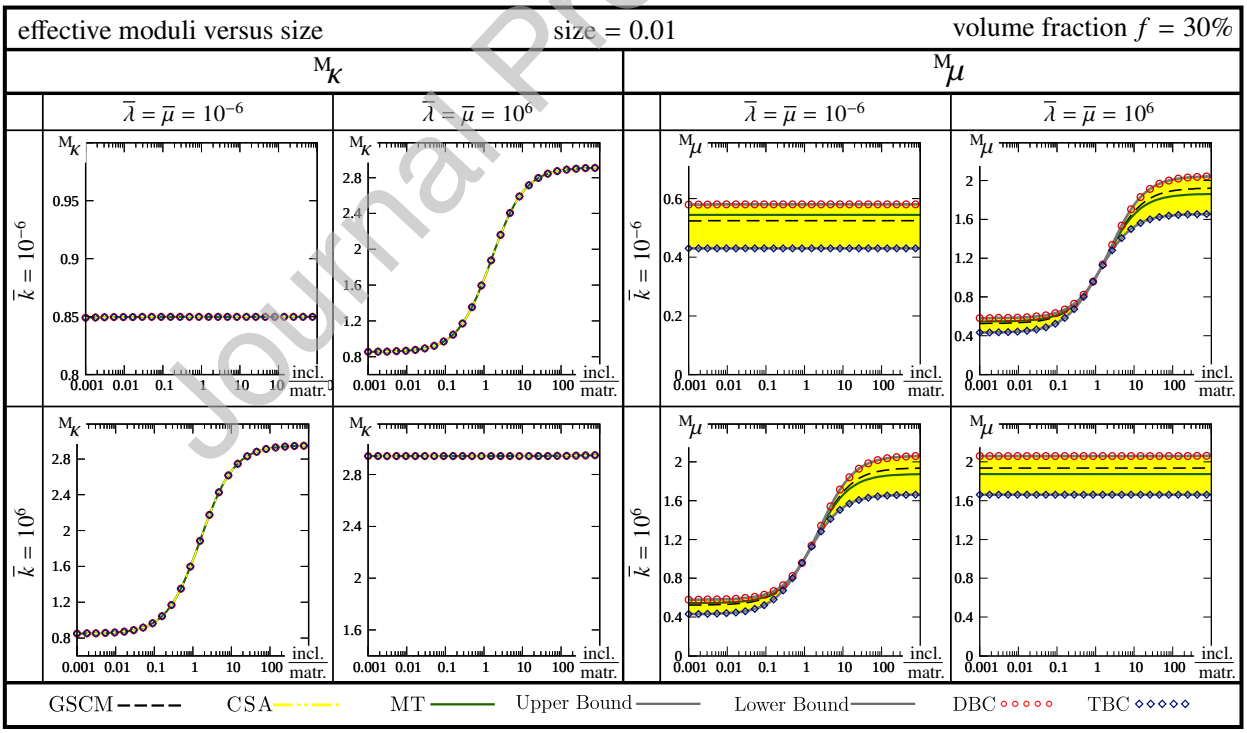

Figure 11: The macroscopic bulk and shear moduli versus the stiffness ratio for size = 0.01. Four extreme cases of interface parameters are considered in order to investigate the neutrality of the material response to the inclusion stiffness.

shear modulus ${}^{\mathrm{M}}\mu$ and they coincide in the case of the overall bulk modulus ${}^{\mathrm{M}}k$ in accordance with the observation made by Hashin and Rosen (1964) for perfect interfaces.

So far the variation of the overall moduli versus size has been investigated for three specific stiffness ratios. In order to accentuate the role of stiffness ratio and investigate the neutrality of the overall response to the inclusion stiffness in the presence of imperfect interfaces, we study the behavior of the overall moduli versus the stiffness ratio in Fig. 11. To highlight the role of the interface, the study is carried out at a small size=0.01. Four extreme cases of

(i) very weak cohesive and very weak elastic interface resistance $\{\ \overline{k} = 10^{-6}\ ,\ \ \overline{\mu} = \overline{\lambda} = 10^{-6}\ \}$,

(ii) very weak cohesive and very strong elastic interface resistance $\{\ \overline{k} = 10^{-6}\ ,\ \ \overline{\mu} = \overline{\lambda} = 10^{6}\ \}$,

(iii) very strong cohesive and very weak elastic interface resistance $\{\ \overline{k} = 10^{6}\ ,\ \ \overline{\mu} = \overline{\lambda} = 10^{-6}\ \}$,

(iv) very strong cohesive and very strong elastic interface resistance $\{\ \overline{k} = 10^{6}\ ,\ \ \overline{\mu} = \overline{\lambda} = 10^{6}\ \}$,

for the interface parameters are considered. Note that the case (iii) in our analysis renders a response similar to that of a perfect interface model, see Fig. 1. More precisely, the general interface model in case (iii) strongly resists against opening representing a perfect bonding between the inclusion and the matrix but also, shows nearly no elastic resistance along the interface similar to the classical first-order homogenization. It is observed that in cases (i) and (iv) where both the elastic and cohesive interface responses are either very weak or very strong, the overall properties show no sensitivity with respect to the inclusion stiffness therefore, the material response becomes neutral to the inclusion. On the other hand, for the two other cases of (ii) and (iii), the overall response varies with the stiffness ratio and stiffer inclusions correspond to a stiffer overall response. The concept of neutrality of mechanical response with respect to thin fibers was presented by Goudarzi and Simone (2019) where both imperfect and perfect bondings between the fibers and matrix were assumed which shall be compared with the discussion here.

As pointed out earlier, a key feature of our proposed modified Mori–Tanaka approach is that in addition to the overall material properties, it determines the interaction tensors and consequently the stress and strain fields within each phase of the medium. The next set of examples are devised to demonstrate the utility of our modified Mori–Tanaka method to calculate the stress state in the medium subject to volumetric expansion and simple shear. Figures 12–14 show the analytical and computational stress distributions throughout the micro-structure for different sizes as well as different stiffness ratios. All of the micro-structures are schematically scaled to the same size for the sake of better illustration. In each figure, the rows correspond to specific stiffness ratios. At the left columns, volumetric expansion is applied to the micro-structure and the pressure-like quantity $[\boldsymbol{\sigma}_{xx} + \boldsymbol{\sigma}_{yy} + \boldsymbol{\sigma}_{zz}]/3$ is more relevant to study. On the other hand, at the right columns, simple shear in xy-plane is applied to the RVE in which case the stress component of interest is $[\boldsymbol{\sigma}]_{xy}$. In each box, the top micro-structures correspond to the computational local stress distributions due

to DBC and TBC and the analytical stress distribution is shown at the center. Since our proposed analytical scheme determines the average stresses in the constituents of the medium, the bottom micro-structures in each box render the average computational stress due to DBC and TBC suitable for comparison with the analytical stresses. The average stresses in the particle and the matrix are stated below each case for the sake of clarity. For the expansion case, the analytical stress field is outstandingly precise and the stress distribution completely resembles the computational and

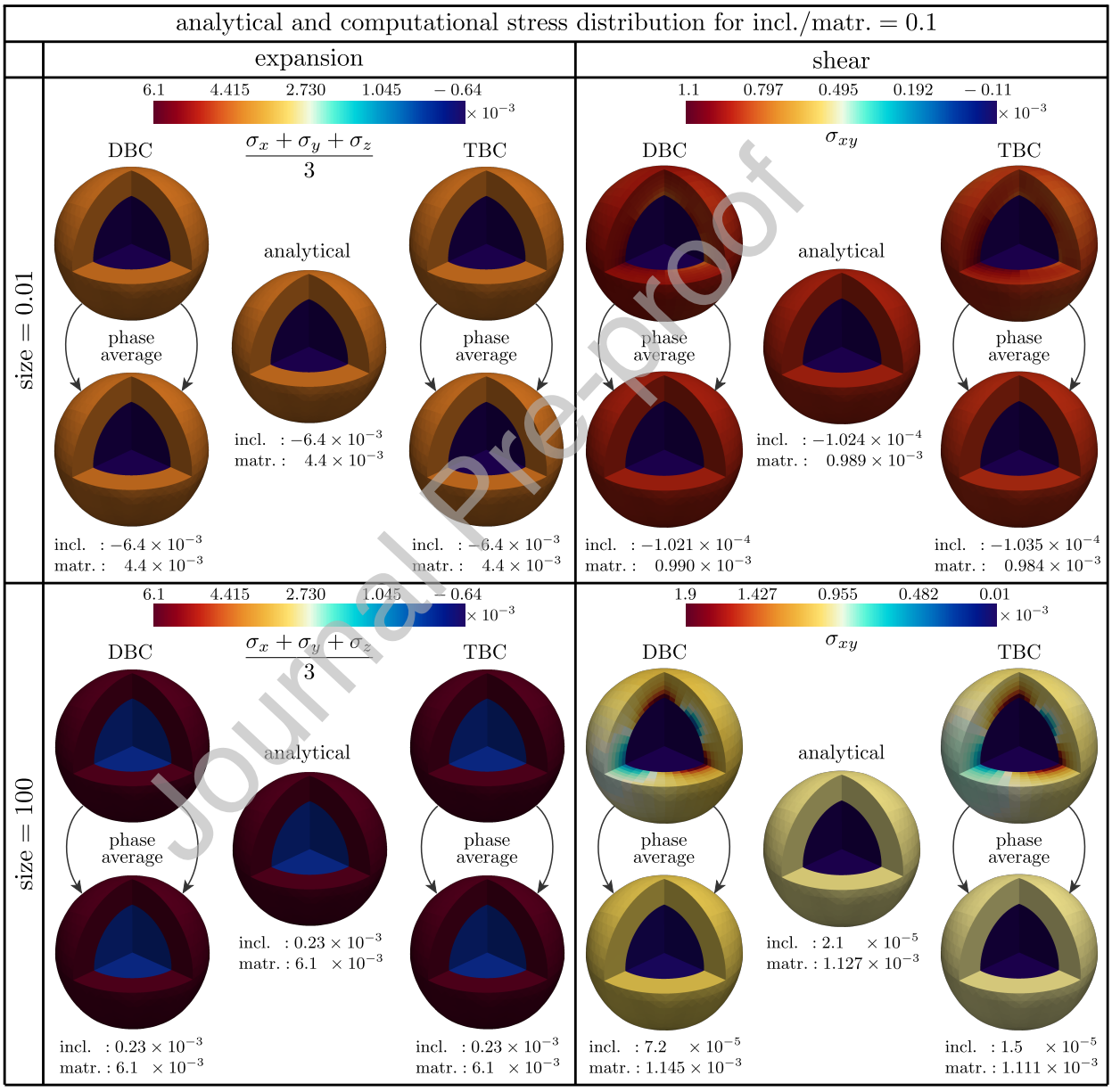

Figure 12: Comparison of the analytical and numerical stress distributions within the RVE at different sizes for incl./matr. = 0.1. On each block, the top micro-structures correspond to the local stress distribution due to DBC and TBC. The analytical stress distribution is shown at the center. The bottom micro-structures render the average of the computational stresses due to DBC and TBC.

average computational stresses. However, for the shear case various conclusions can be drawn. For incl./matr. = 0.1, the average stresses due to DBC overestimate the analytical stresses both in the matrix and particle. On the other hand, the average stresses due to TBC underestimate the analytical stresses both in the matrix and particle. When incl./matr. = 1, for size = 0.01, the computational average stresses due to DBC and TBC overestimate and underestimate the analytical stresses in both phases, respectively. When size = 100, the same result holds for the average

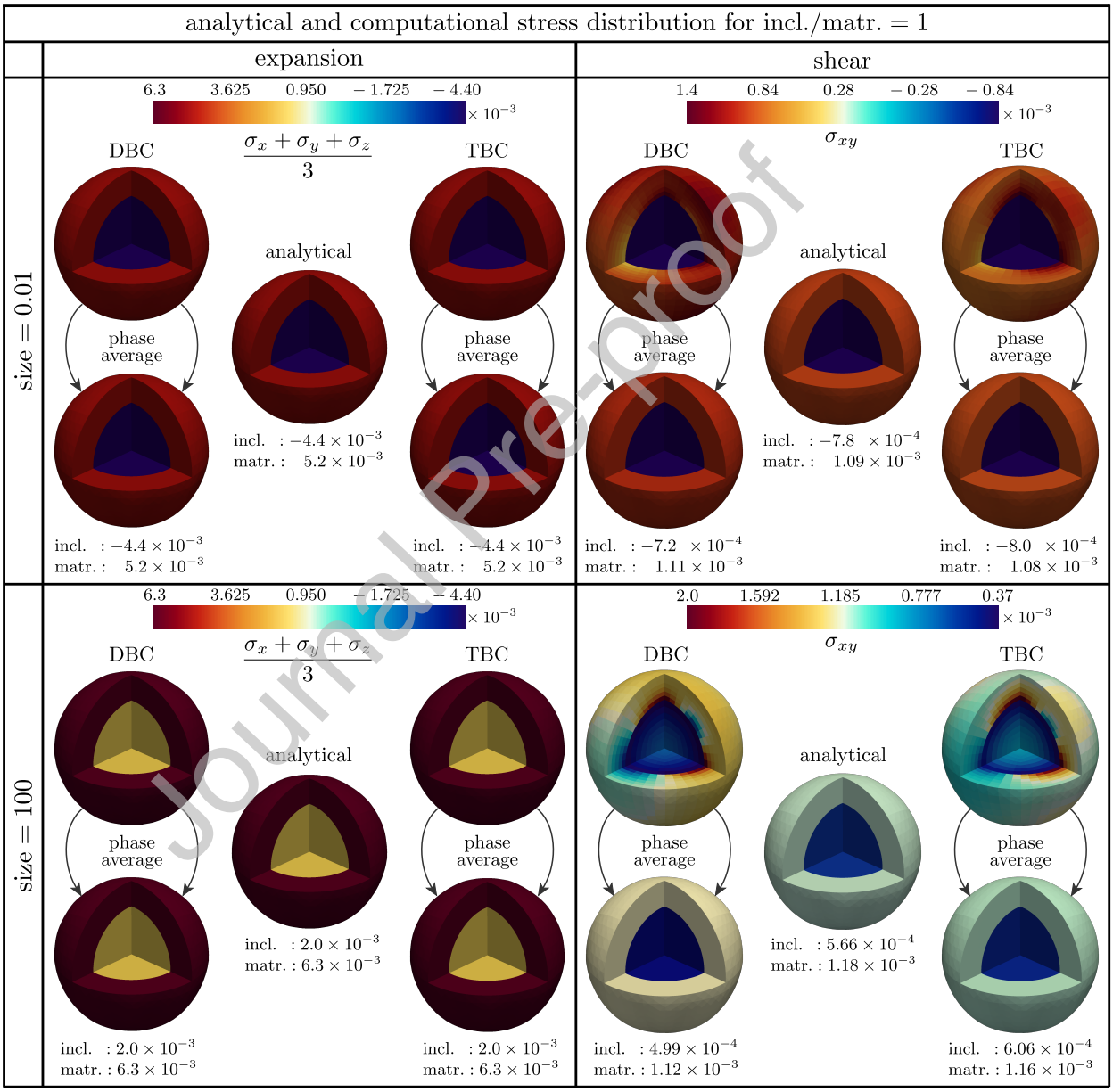

Figure 13: Comparison of the analytical and numerical stress distributions within the RVE at different sizes for incl./matr. = 1. On each block, the top micro-structures correspond to the local stress distribution due to DBC and TBC. The analytical stress distribution is shown at the center. The bottom micro-structures render the average of the computational stresses due to DBC and TBC.

stress in the matrix. However, the average stress in the fiber due to TBC overestimate the analytical stress with DBC underestimating it. Finally, for incl./matr. = 10, the computational average stresses similarly overestimate and underestimate the analytical stresses when size = 0.01. DBC results in the least average stress in the matrix where as TBC yields the highest value when size = 100.

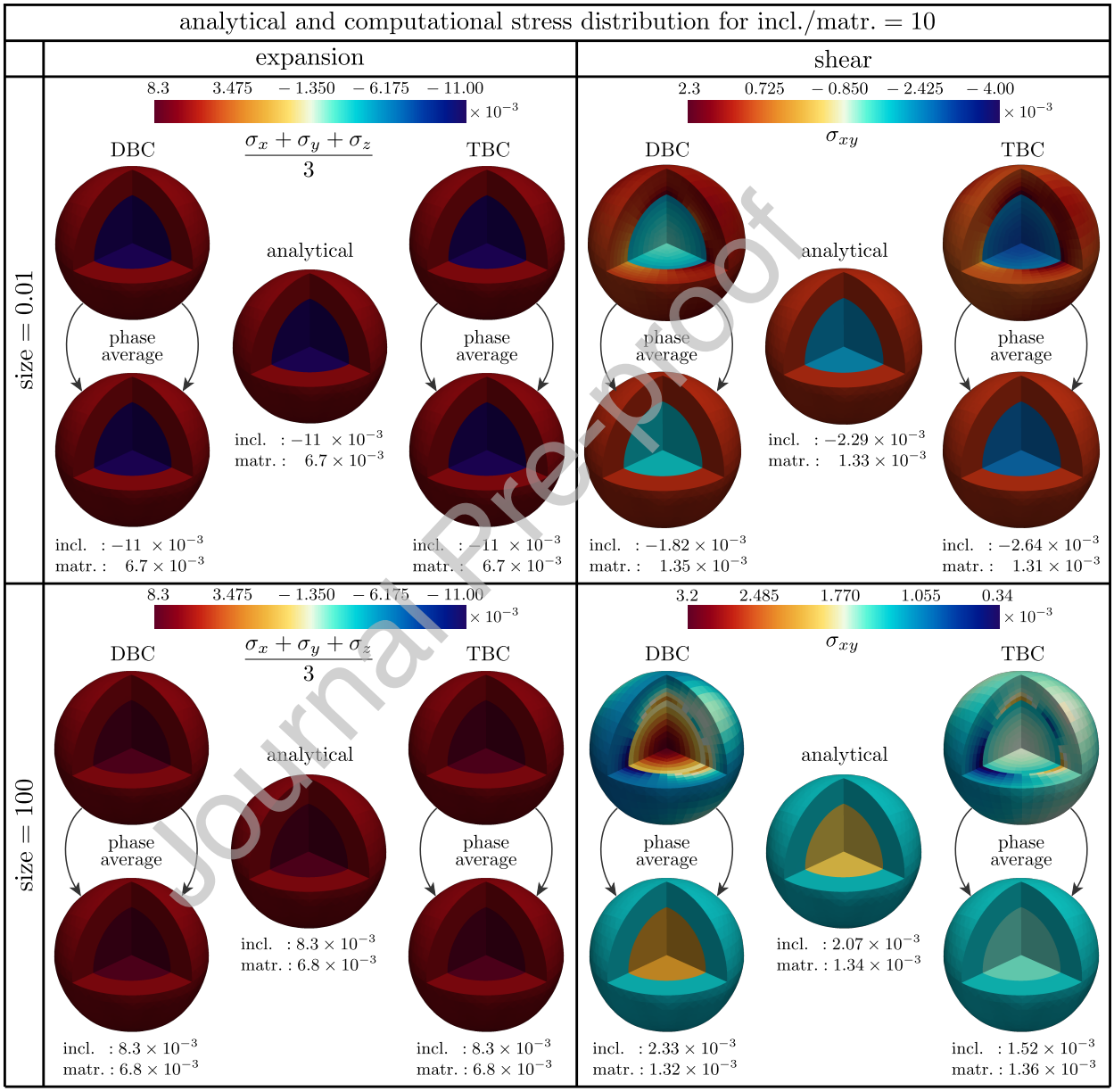

Figure 14: Comparison of the analytical and numerical stress distributions within the RVE at different sizes for incl./matr. = 10. On each block, the top micro-structures correspond to the local stress distribution due to DBC and TBC. The analytical stress distribution is shown at the center. The bottom micro-structures render the average of the computational stresses due to DBC and TBC.

5. Discussion and comparison with literature

In this section, we carry out a comprehensive comparison between our results and the available analytical estimates in the literature for the elastic and cohesive interfaces. In doing so, the overall moduli of particulate composites are examined for various stiffness ratios at different sizes. As mentioned earlier, suitable choices of the general interface parameters can recover any of elastic, cohesive or perfect interfaces, see Fig. 1 for more clarity. The elastic (stress-type) interface model here is recovered by setting $\overline{k} \to \infty$ in our general interface model. On the contrary, the cohesive (spring-type) interface model is recovered by setting $\overline{\lambda} = 0$ and $\overline{\mu} = 0$. Our explicit expressions for the bulk modulus in these limit cases reduce to

elastic interface model:
$$^{\mathrm{M}}\kappa = \frac{3r_1\Big[\kappa_2[3\kappa_1 + 4\mu_2] + 4f\mu_2[\kappa_1 - \kappa_2]\Big] + 4\Big[\overline{\lambda} + \overline{\mu}\Big]\Big[3\kappa_2 + 4f\mu_2\Big]}{3r_1\Big[3\kappa_1 + 4\mu_2 + 3f[\kappa_2 - \kappa_1]\Big] + 12\Big[1 - f\Big]\Big[\overline{\lambda} + \overline{\mu}\Big]}. \tag{64}$$

cohesive interface model:
$$^{\mathrm{M}}\kappa = \frac{\overline{k}r_1\Big[\kappa_2[3\kappa_1 + 4\mu_2] + 4f\mu_2[\kappa_1 - \kappa_2]\Big] + 12\kappa_1\kappa_2\mu_2\Big[1 - f\Big]}{\overline{k}r_1\Big[3\kappa_1 + 4\mu_2 + 3f[\kappa_2 - \kappa_1]\Big] + 3\kappa_1\Big[4\mu_2 + 3\kappa_2\Big]}. \tag{65}$$

For the shear modulus, the final expressions for the bounds and estimate (Eqs. (28), (33) and (39)) remain the same, however, special treatments are required while assembling the corresponding matrices in Eqs. (A.1), (A.3) and (A.6). For the sake of brevity, we omit the associated derivations for shear modulus as it does not render a short closed-form explicit solution. Figure 15 shows the effective moduli versus size for various stiffness ratios for the elastic interface parameters of $\overline{\lambda} = \overline{\mu} = 1$. In this example, we compare our results with four other analytical estimates developed in (Duan et al., 2005, 2007; Gu et al., 2014; Zemlyanova and Mogilevskaya, 2018). Note, the framework developed by Zemlyanova and Mogilevskaya (2018) accounts for the Steigmann–Ogden model, but we simplified it to the Gurtin–Murdoch interface model suitable for the comparison, see also (Kushch et al., 2013). We observe an excellent agreement between all the solutions for the bulk modulus. For the case of shear modulus, a remarkable agreement is observed between our generalized self-consistent method and the solution proposed by Duan et al. (2007) and Gu et al. (2014). Our Mori–Tanaka method also coincides with the solution developed by Duan et al. (2005). Moreover, the solution developed by Zemlyanova and Mogilevskaya (2018) coincides with the lower bound at small sizes and tends to converge to the Mori–Tanaka method as the size increases. It is noteworthy that the closed-form expression for the *bulk modulus* proposed by Nazarenko et al. (2017) is also in perfect accordance with these results. Figure 16 shows the effective moduli versus size for various stiffness ratios for the cohesive interface parameter of $\overline{k} = 1$. In this example, we compare our results with two other analytical estimates developed by Duan et al. (2007) and Gu et al. (2014). Similar to the previous case, all the results coincide for the case of bulk modulus. For the shear modulus,

there is a remarkable agreement our generalized self-consistent method and the solution proposed by Duan et al. (2007) and Gu et al. (2014). It shall be noted that Duan et al. (2005) obtain the effective properties using three different types of micromechanics schemes, i.e. the Mori–Tanaka method (MTM), the composite spheres assemblage (CSA) and the generalized self-consistent method (GSCM). On the other hand, Gu et al. (2014), Duan et al. (2007) and Zemlyanova and Mogilevskaya (2018) use a two-step procedure as follows. Firstly, they identify an *equivalent particle* that substitutes the particle-plus-interface and secondly, they utilize standard homogenization schemes. In the second step though, Gu et al. (2014) and Duan et al. (2007) consider the GSCM, while Zemlyanova and Mogilevskaya (2018) utilize the Maxwell's homogenization approach. For further details about Maxwell's homogenization approach

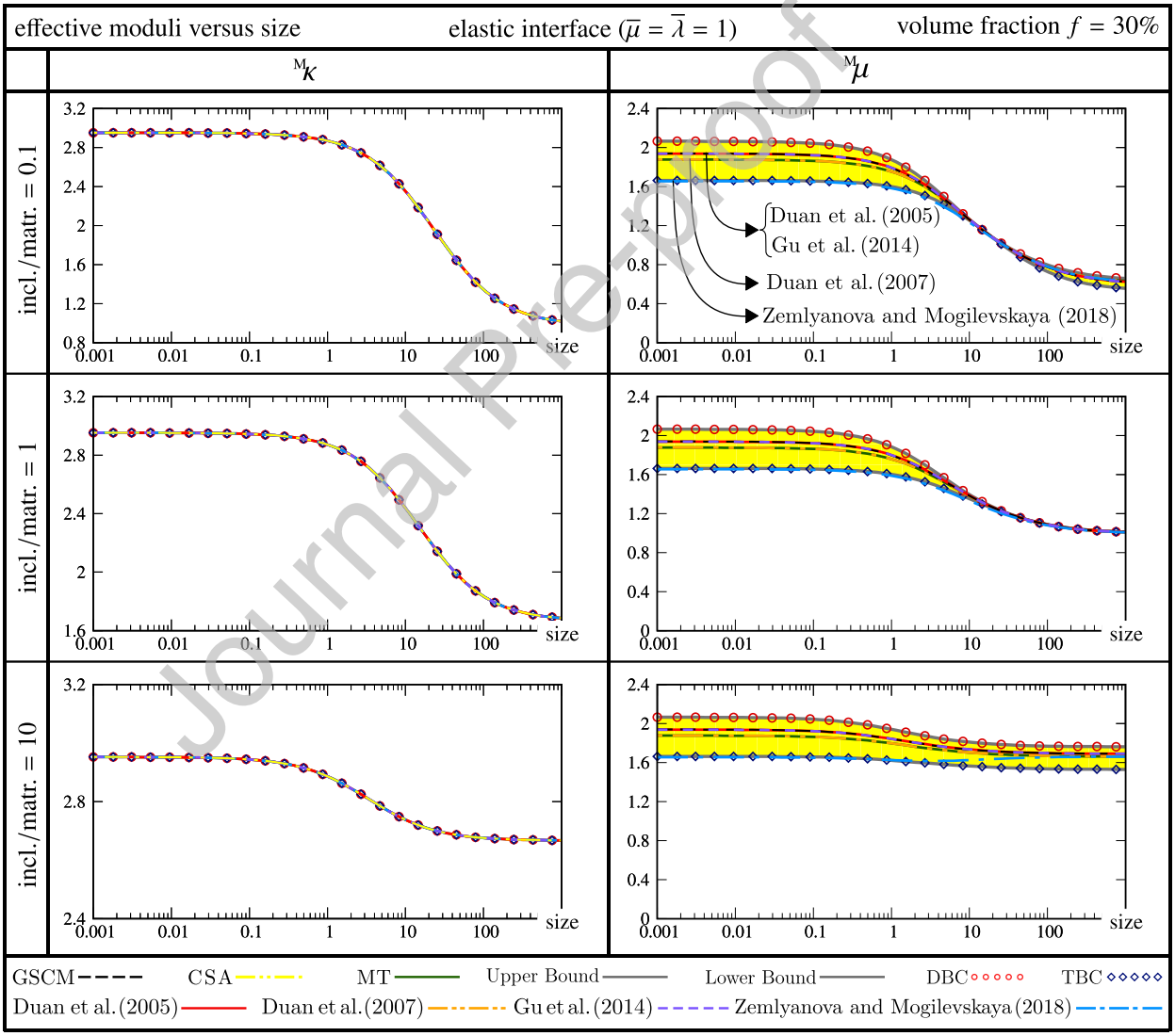

Figure 15: Comparison of the overall moduli for the elastic interface with the available closed-form expressions in the literature.

and its utility for a broad range of applications, see Sevostianov et al. (2019). It is well-established that the *effective bulk modulus* of a particle reinforced composite obtained with Maxwell's scheme is identical to that obtained with all the other classical homogenization schemes. This property explains the excellent agreement between the results from all various homogenization techniques on the left column of Fig. 15. On the other hand, Maxwell-based estimates for the *effective shear modulus* are different from those obtained with generalized self-consistent type schemes. This feature explains the difference between the results on the right column of Fig. 15. In the classical case, the Maxwell-based estimates coincide with the expressions for the lower Hashin–Shtrikman bound if the particles are stiffer than the matrix. On the contrary, if the matrix is stiffer than the particles, the Maxwell-based estimates coincide with the

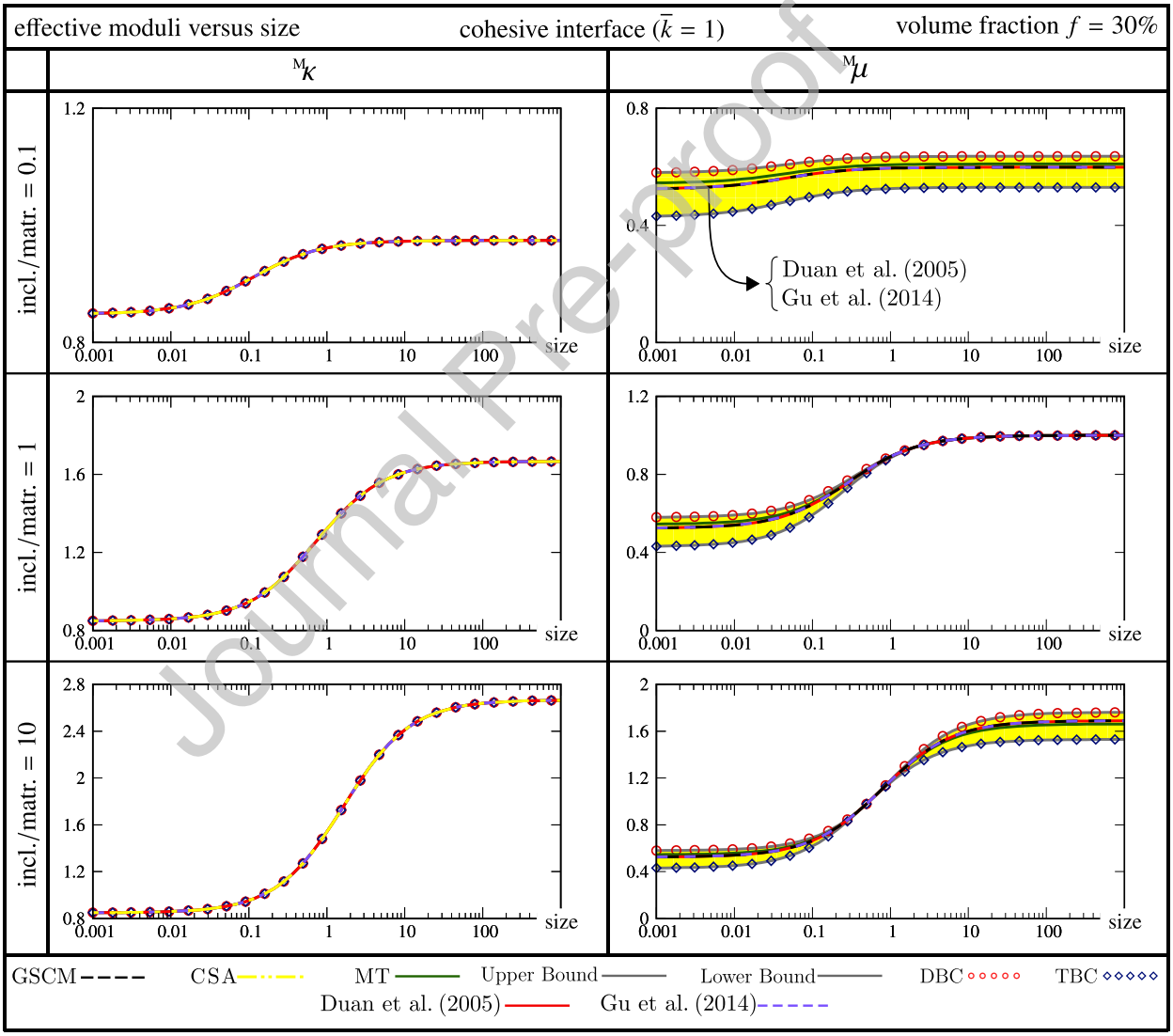

Figure 16: Comparison of the overall moduli for the cohesive interface with the available closed-form expressions in the literature.

expressions for the upper Hashin–Shtrikman bound. This property seems to remain valid even in the presence of generalized interfaces between the matrix and particles. Note that a key feature of this contribution is to verify the analytical estimates with computational simulations using the finite element method, for the first time.

6. Conclusion

We established two novel techniques to determine the overall behavior of particulate composites via extending homogenization to account for general interfaces hence, size effects. An interface-enhanced composite cylinder assemblage (CSA) approach and generalized self-consistent method (GSCM) were developed to incorporate interfaces resulting in estimates and bounds for the effective properties of composites. Explicit formulations for the overall bulk modulus and semi-explicit formulations for the overall shear modulus of particulate composites accounting for general interfaces were presented for the first time. Afterwards, we developed a generalized interface enhanced Mori-Tanaka to study size effects in particulate composites, verified by numerical computations. This approach not only provides estimates for the overall properties, but also identifies concentration tensors in all phases of the composite. As a result, the state of stress and strain in the matrix, particle and the interface can be determined which provides a significant insight into the computational design of composites accounting for generalized interfaces and size effects. A perfect agreement is observed between the proposed analytical estimates and the computational results obtained using the finite element method. Our proposed methodology is versatile and can recover any of elastic, cohesive or perfect interface models. All of the observations demonstrate that the overall material response in the presence of the general interface is, in principle, complicated. We believe that this manuscript deepens our understanding of the interface effects and size-dependent behavior of composites which paves the way towards computational metamaterial design.

Appendix A. System of equations for the estimate and bounds on the shear modulus

In this section we elaborate on the system of equations used to obtain the estimate and the bounds on the macroscopic shear modulus explained in Section 3.2.

Appendix A.1. Strain bound on the shear modulus

The displacement fields in the matrix and the particle were given in Eq. (24) which has eight unknowns of $\Xi_1^{(1)}$, $\Xi_2^{(1)}$, $\Xi_3^{(1)}$, $\Xi_4^{(1)}$, $\Xi_1^{(2)}$, $\Xi_2^{(2)}$, $\Xi_3^{(2)}$ and $\Xi_4^{(2)}$. We concluded that since the displacement fields at the center of the RVE must be finite, $\Xi_3^{(1)}$ and $\Xi_4^{(1)}$ must vanish. For the remaining six unknowns we apply the boundary and interface conditions (25)

resulting in the below system of equations

$$\begin{bmatrix}
1+\frac{\mu_1}{\bar{k}r_1} & 2-3\frac{\kappa_1}{\mu_1}+\zeta_1 & -1+\frac{\mu_2}{\bar{k}r_1} & -2+3\frac{\kappa_2}{\mu_2}+\zeta_2 & -3-\frac{12\mu_2}{\bar{k}r_1} & -3-3\frac{\kappa_2}{\mu_2}+\zeta_3 \\
1+\frac{\mu_1}{\bar{k}r_1} & -\frac{11}{3}-5\frac{\kappa_1}{\mu_1}+\zeta_4 & -1+\frac{\mu_2}{\bar{k}r_1} & \frac{11}{3}+5\frac{\kappa_2}{\mu_2}+\zeta_5 & 2+\frac{8\mu_2}{\bar{k}r_1} & -2+\frac{3\kappa_2}{\bar{k}r_1} \\
2\mu_1-\frac{\overline{\lambda}+\overline{\mu}}{r_1} & 3\kappa_1-2\mu_1+\zeta_6 & -2\mu_2-\frac{\overline{\lambda}+\overline{\mu}}{r_1} & -3\kappa_2+2\mu_2+\zeta_7 & 24\mu_2+\frac{12[\overline{\lambda}+\overline{\mu}]}{r_1} & 18\kappa_2+8\mu_2+\frac{6\kappa_2[\overline{\lambda}+\overline{\mu}]}{\mu_2 r_1} \\
2\mu_1+\zeta_8 & -16\kappa_1-\frac{10}{3}\mu_1+\zeta_9 & -2\mu_2+\zeta_8 & 16\kappa_2+\frac{10}{3}\mu_2+\zeta_{10} & -16\mu_2+\zeta_{11} & -6\kappa_2+\zeta_{12} \\
0 & 0 & 1 & \left[2-3\frac{\kappa_2}{\mu_2}\right]f^{-2/3} & 3f^{5/3} & \left[3+3\frac{\kappa_2}{\mu_2}\right]f \\
0 & 0 & 1 & -\left[\frac{11}{3}+5\frac{\kappa_2}{\mu_2}\right]f^{-2/3} & -2f^{5/3} & 2f
\end{bmatrix}
\begin{bmatrix} \Xi_1^{(1)} \\ \Xi_2^{(1)} \\ \Xi_1^{(2)} \\ \Xi_2^{(2)} \\ \Xi_3^{(2)} \\ \Xi_4^{(2)} \end{bmatrix}
=
\begin{bmatrix} 0 \\ 0 \\ 0 \\ 0 \\ 1 \\ 1 \end{bmatrix}, \quad \text{(A.1)}$$

with

$$\begin{aligned}
\zeta_1 &= \frac{3\kappa_1-2\mu_1}{2\bar{k}r_1}, & \zeta_5 &= -\frac{24\kappa_2+5\mu_2}{3\bar{k}r_1}, & \zeta_9 &= -\frac{\kappa_1\left[9\overline{\lambda}+19\overline{\mu}\right]}{\mu_1 r_1}-\frac{\left[45\overline{\lambda}+67\overline{\mu}\right]}{3r_1}, \\
\zeta_2 &= \frac{3\kappa_2-2\mu_2}{2\bar{k}r_1}, & \zeta_6 &= \frac{[9\kappa_1+15\mu_1]\left[\overline{\lambda}+\overline{\mu}\right]}{\mu_1 r_1}, & \zeta_{10} &= -\frac{\kappa_2\left[9\overline{\lambda}+19\overline{\mu}\right]}{\mu_2 r_1}-\frac{\left[45\overline{\lambda}+67\overline{\mu}\right]}{3r_1}, \\
\zeta_3 &= -\frac{9\kappa_2+4\mu_2}{\bar{k}r_1}, & \zeta_7 &= \frac{[9\kappa_2+15\mu_2]\left[\overline{\lambda}+\overline{\mu}\right]}{\mu_2 r_1}, & \zeta_{11} &= -\frac{4\left[3\overline{\lambda}+4\overline{\mu}\right]}{r_1}, \\
\zeta_4 &= -\frac{24\kappa_1+5\mu_1}{3\bar{k}r_1}, & \zeta_8 &= \frac{\left[\overline{\lambda}+\overline{\mu}\right]+2\overline{\mu}}{r_1}, & \zeta_{12} &= \frac{-6\kappa_2\left[\overline{\lambda}+\overline{\mu}\right]+4\mu_2\overline{\mu}}{\mu_2 r_1}.
\end{aligned} \quad \text{(A.2)}$$

Appendix A.2. Stress bound on shear modulus

The far field stress field in this case led to the displacement field according to Eq. (24) with the eight unknowns $\Xi_1^{(1)}$, $\Xi_2^{(1)}$, $\Xi_3^{(1)}$, $\Xi_4^{(1)}$, $\Xi_1^{(2)}$, $\Xi_2^{(2)}$, $\Xi_3^{(2)}$ and $\Xi_4^{(2)}$. We concluded that since the displacement fields at the center of the RVE must be finite, $\Xi_3^{(1)}$ and $\Xi_4^{(1)}$ must vanish. For the remaining six unknowns we apply the boundary and interface conditions (30) resulting in the below system of equations

$$\begin{bmatrix}
1+\frac{\mu_1}{\bar{k}r_1} & 2-3\frac{\kappa_1}{\mu_1}+\zeta_1 & -1+\frac{\mu_2}{\bar{k}r_1} & -2+3\frac{\kappa_2}{\mu_2}+\zeta_2 & -3-\frac{12\mu_2}{\bar{k}r_1} & -3-3\frac{\kappa_2}{\mu_2}+\zeta_3 \\
1+\frac{\mu_1}{\bar{k}r_1} & -\frac{11}{3}-5\frac{\kappa_1}{\mu_1}+\zeta_4 & -1+\frac{\mu_2}{\bar{k}r_1} & \frac{11}{3}+5\frac{\kappa_2}{\mu_2}+\zeta_5 & 2+\frac{8\mu_2}{\bar{k}r_1} & -2+\frac{3\kappa_2}{\bar{k}r_1} \\
2\mu_1-\frac{\overline{\lambda}+\overline{\mu}}{r_1} & 3\kappa_1-2\mu_1+\zeta_6 & -2\mu_2-\frac{\overline{\lambda}+\overline{\mu}}{r_1} & -3\kappa_2+2\mu_2+\zeta_7 & 24\mu_2+\frac{12[\overline{\lambda}+\overline{\mu}]}{r_1} & 18\kappa_2+8\mu_2+\frac{6\kappa_2[\overline{\lambda}+\overline{\mu}]}{\mu_2 r_1} \\
2\mu_1+\zeta_8 & -16\kappa_1-\frac{10}{3}\mu_1+\zeta_9 & -2\mu_2+\zeta_8 & 16\kappa_2+\frac{10}{3}\mu_2+\zeta_{10} & -16\mu_2+\zeta_{11} & -6\kappa_2+\zeta_{12} \\
0 & 0 & 2\mu_2 & [3\kappa_2-2\mu_2]f^{-2/3} & -24\mu_2 f^{5/3} & -[18\kappa_2+8\mu_2]f \\
0 & 0 & 2\mu_2 & -\left[16\kappa_2+\frac{10}{3}\mu_2\right]f^{-2/3} & 16\mu_2 f^{5/3} & 6\kappa_2 f
\end{bmatrix}
\begin{bmatrix} \Xi_1^{(1)} \\ \Xi_2^{(1)} \\ \Xi_1^{(2)} \\ \Xi_2^{(2)} \\ \Xi_3^{(2)} \\ \Xi_4^{(2)} \end{bmatrix}
=
\begin{bmatrix} 0 \\ 0 \\ 0 \\ 0 \\ 1 \\ 1 \end{bmatrix}, \quad \text{(A.3)}$$

with

$$
\begin{aligned}
\zeta_1 &= \frac{3\kappa_1 - 2\mu_1}{2\overline{k}r_1}, \qquad \zeta_5 = -\frac{24\kappa_2 + 5\mu_2}{3\overline{k}r_1}, \qquad \zeta_9 = -\frac{\kappa_1\left[9\overline{\lambda} + 19\overline{\mu}\right]}{\mu_1 r_1} - \frac{\left[45\overline{\lambda} + 67\overline{\mu}\right]}{3r_1},\\
\zeta_2 &= \frac{3\kappa_2 - 2\mu_2}{2\overline{k}r_1}, \qquad \zeta_6 = \frac{[9\kappa_1 + 15\mu_1]\left[\overline{\lambda} + \overline{\mu}\right]}{\mu_1 r_1}, \qquad \zeta_{10} = -\frac{\kappa_2\left[9\overline{\lambda} + 19\overline{\mu}\right]}{\mu_2 r_1} - \frac{\left[45\overline{\lambda} + 67\overline{\mu}\right]}{3r_1},\\
\zeta_3 &= -\frac{9\kappa_2 + 4\mu_2}{\overline{k}r_1}, \qquad \zeta_7 = \frac{[9\kappa_2 + 15\mu_2]\left[\overline{\lambda} + \overline{\mu}\right]}{\mu_2 r_1}, \qquad \zeta_{11} = -\frac{4\left[3\overline{\lambda} + 4\overline{\mu}\right]}{r_1},\\
\zeta_4 &= -\frac{24\kappa_1 + 5\mu_1}{3\overline{k}r_1}, \qquad \zeta_8 = \frac{\left[\overline{\lambda} + \overline{\mu}\right] + 2\overline{\mu}}{r_1}, \qquad \zeta_{12} = \frac{-6\kappa_2\left[\overline{\lambda} + \overline{\mu}\right] + 4\mu_2\overline{\mu}}{\mu_2 r_1}.
\end{aligned}
\tag{A.4}
$$

Appendix A.3. Effective shear modulus

For this problem the displacement fields in the particle and the matrix are given in Eq. (24) and the displacement field in the effective medium is given in Eq. (35). This problem contains ten unknown of $\Xi_1^{(1)}$, $\Xi_2^{(1)}$, $\Xi_3^{(1)}$, $\Xi_4^{(1)}$, $\Xi_1^{(2)}$, $\Xi_2^{(2)}$, $\Xi_3^{(2)}$, $\Xi_4^{(2)}$, $\Xi_3^{(\mathrm{eff})}$ and $\Xi_4^{(\mathrm{eff})}$. We concluded that since at the center of the RVE the displacement field needs to be finite, $\Xi_3^{(1)}$ and $\Xi_4^{(1)}$ must be zero. Substitution of the stress and displacement fields in Eq. (38) yielded $\Xi_4^{(\mathrm{eff})} = 0$. For the remaining unknowns we apply the boundary and interface conditions (37) resulting in the below system of equations

$$
\boldsymbol{Q}\begin{bmatrix} \Xi_1^{(1)} \\ \Xi_2^{(1)} \\ \Xi_1^{(2)} \\ \Xi_2^{(2)} \\ \Xi_3^{(2)} \\ \Xi_4^{(2)} \end{bmatrix} = \begin{bmatrix} 0 \\ 0 \\ 0 \\ 0 \\ 1 \\ 1 \end{bmatrix} + \begin{bmatrix} 0 \\ 0 \\ 0 \\ 0 \\ 3 \\ -2 \end{bmatrix} f^{5/3}\,\Xi_3^{\mathrm{eff}},
\tag{A.5}
$$

where

$$\boldsymbol{Q}=\begin{bmatrix} 1+\frac{\mu_1}{\bar{k}r_1} & 2-3\frac{\kappa_1}{\mu_1}+\zeta_1 & -1+\frac{\mu_2}{\bar{k}r_1} & -2+3\frac{\kappa_2}{\mu_2}+\zeta_2 & -3-\frac{12\mu_2}{\bar{k}r_1} & -3-3\frac{\kappa_2}{\mu_2}+\zeta_3 \\ 1+\frac{\mu_1}{\bar{k}r_1} & -\frac{11}{3}-5\frac{\kappa_1}{\mu_1}+\zeta_4 & -1+\frac{\mu_2}{\bar{k}r_1} & \frac{11}{3}+5\frac{\kappa_2}{\mu_2}+\zeta_5 & 2+\frac{8\mu_2}{\bar{k}r_1} & -2+\frac{3\kappa_2}{\bar{k}r_1} \\ 2\mu_1-\frac{\overline{\lambda}+\overline{\mu}}{r_1} & 3\kappa_1-2\mu_1+\zeta_6 & -2\mu_2-\frac{\overline{\lambda}+\overline{\mu}}{r_1} & -3\kappa_2+2\mu_2+\zeta_7 & 24\mu_2+\frac{12\left[\overline{\lambda}+\overline{\mu}\right]}{r_1} & 18\kappa_2+8\mu_2+\frac{6\kappa_2\left[\overline{\lambda}+\overline{\mu}\right]}{\mu_2 r_1} \\ 2\mu_1+\zeta_8 & -16\kappa_1-\frac{10}{3}\mu_1+\zeta_9 & -2\mu_2+\zeta_8 & 16\kappa_2+\frac{10}{3}\mu_2+\zeta_{10} & -16\mu_2+\zeta_{11} & -6\kappa_2+\zeta_{12} \\ 0 & 0 & 1 & \left[2-3\frac{\kappa_2}{\mu_2}\right]f^{-2/3} & 3f^{5/3} & \left[3+3\frac{\kappa_2}{\mu_2}\right]f \\ 0 & 0 & 1 & -\left[\frac{11}{3}+5\frac{\kappa_2}{\mu_2}\right]f^{-2/3} & -2f^{5/3} & 2f \end{bmatrix}, \tag{A.6}$$

with

$$\begin{aligned} \zeta_1&=\frac{3\kappa_1-2\mu_1}{2\bar{k}r_1}, & \zeta_5&=-\frac{24\kappa_2+5\mu_2}{3\bar{k}r_1}, & \zeta_9&=-\frac{\kappa_1\left[9\overline{\lambda}+19\overline{\mu}\right]}{\mu_1 r_1}-\frac{\left[45\overline{\lambda}+67\overline{\mu}\right]}{3r_1}, \\ \zeta_2&=\frac{3\kappa_2-2\mu_2}{2\bar{k}r_1}, & \zeta_6&=\frac{[9\kappa_1+15\mu_1]\left[\overline{\lambda}+\overline{\mu}\right]}{\mu_1 r_1}, & \zeta_{10}&=-\frac{\kappa_2\left[9\overline{\lambda}+19\overline{\mu}\right]}{\mu_2 r_1}-\frac{\left[45\overline{\lambda}+67\overline{\mu}\right]}{3r_1}, \\ \zeta_3&=-\frac{9\kappa_2+4\mu_2}{\bar{k}r_1}, & \zeta_7&=\frac{[9\kappa_2+15\mu_2]\left[\overline{\lambda}+\overline{\mu}\right]}{\mu_2 r_1}, & \zeta_{11}&=-\frac{4\left[3\overline{\lambda}+4\overline{\mu}\right]}{r_1}, \\ \zeta_4&=-\frac{24\kappa_1+5\mu_1}{3\bar{k}r_1}, & \zeta_8&=\frac{\left[\overline{\lambda}+\overline{\mu}\right]+2\overline{\mu}}{r_1}, & \zeta_{12}&=\frac{-6\kappa_2\left[\overline{\lambda}+\overline{\mu}\right]+4\mu_2\overline{\mu}}{\mu_2 r_1}. \end{aligned} \tag{A.7}$$

The obtained system of equations though is nonlinear hence, requiring a special treatment. We express the solution of the above system in the form

$$\begin{bmatrix} \Xi_1^{(1)} \\ \Xi_2^{(1)} \\ \Xi_1^{(2)} \\ \Xi_2^{(2)} \\ \Xi_3^{(2)} \\ \Xi_4^{(2)} \end{bmatrix}=\begin{bmatrix} g_1 \\ g_2 \\ a_1 \\ a_2 \\ a_3 \\ a_4 \end{bmatrix}+\begin{bmatrix} h_1 \\ h_2 \\ b_1 \\ b_2 \\ b_3 \\ b_4 \end{bmatrix} f^{5/3}\Xi_3^{(\mathrm{eff})}. \tag{A.8}$$

Using (A.8), the last two conditions of Eq. (36) are written as

$$a_5 + b_5\, f^{5/3}\, \Xi_3^{(\mathrm{eff})} = 2^{\mathrm{M}}\mu - 24\,{}^{\mathrm{M}}\mu\, f^{5/3}\, \Xi_3^{(\mathrm{eff})}\,, \qquad a_6 + b_6\, f^{5/3}\, \Xi_3^{(\mathrm{eff})} = 2^{\mathrm{M}}\mu + 16\,{}^{\mathrm{M}}\mu\, f^{5/3}\, \Xi_3^{(\mathrm{eff})}\,, \tag{A.9}$$

with

$$\begin{aligned}
a_5 &= 2\mu_2 a_1 + [3\kappa_2 - 2\mu_2] f^{-2/3} a_2 - 24\mu_2 f^{5/3} a_3 - [18\kappa_2 + 8\mu_2] f\, a_4\,,\\
a_6 &= 2\mu_2 a_1 - \left[16\kappa_2 + \frac{10}{3}\mu_2\right] f^{-2/3} a_2 + 16\mu_2 f^{5/3} a_3 + 6\kappa_2 f\, a_4\,,\\
b_5 &= 2\mu_2 b_1 + [3\kappa_2 - 2\mu_2] f^{-2/3} b_2 - 24\mu_2 f^{5/3} b_3 - [18\kappa_2 + 8\mu_2] f\, b_4\,,\\
b_6 &= 2\mu_2 b_1 - \left[16\kappa_2 + \frac{10}{3}\mu_2\right] f^{-2/3} b_2 + 16\mu_2 f^{5/3} b_3 + 6\kappa_2 f\, b_4.
\end{aligned} \tag{A.10}$$

Subtracting $(A.9)_1$ from $(A.9)_2$ gives

$$f^{5/3}\Xi_3^{(\mathrm{eff})} = \frac{a_6 - a_5}{40^{\mathrm{M}}\mu + b_5 - b_6}. \tag{A.11}$$

Substituting the final result in $(A.9)_1$, after some algebra we obtain the below quadratic equation

$$80^{\mathrm{M}}\mu^2 - 2[b_6 - b_5 + 12a_6 + 8a_5]^{\mathrm{M}}\mu + a_5 b_6 - b_5 a_6 = 0\,. \tag{A.12}$$

From the two possible solutions the positive value is the macroscopic shear modulus.

References

References

Alfano, G. and Crisfield, M. A. (2001). Finite element interface models for the delamination analysis of laminated composites: Mechanical and computational issues. *International Journal for Numerical Methods in Engineering*, 50:1701–1736.

Altenbach, H. and Eremeyev, V. A. (2011). On the shell theory on the nanoscale with surface stresses. *International Journal of Engineering Science*, 49:1294–1301.

Barenblatt, G. I. (1959). The formation of equilibrium cracks during brittle fracture. General ideas and hypotheses. Axially-symmetric cracks. *Journal of Applied Mathematics and Mechanics*, 23:622–636.

Barenblatt, G. I. (1962). The Mathematical Theory of Equilibrium of Crack in Brittle Fracture. *Advances in Applied Mechanics*, 7:55–129.

Benveniste, Y. (2006). A general interface model for a three-dimensional curved thin anisotropic interphase between two anisotropic media. *Journal of the Mechanics and Physics of Solids*, 54:708–734.

Benveniste, Y., Dvorak, G. J., and Chen, T. (1989). Stress fields in composites with coated inclusions. *Mechanics of Materials*, 7:305–317.

Benveniste, Y. and Miloh, T. (2001). Imperfect soft and stiff interfaces in two-dimensional elasticity. *Mechanics of Materials*, 33:309–323.

Brassart, L., Inglis, H. M., Delannay, L., Doghri, I., and Geubelle, P. H. (2009). An extended Mori-Tanaka homogenization scheme for finite strain modeling of debonding in particle-reinforced elastomers. *Computational Materials Science*, 45:611–616.

Brisard, S., Dormieux, L., and Kondo, D. (2010). Hashin-Shtrikman bounds on the shear modulus of a nanocomposite with spherical inclusions and interface effects. *Computational Materials Science*, 50:403–410.

Charalambakis, N., Chatzigeorgiou, G., Chemisky, Y., and Meraghni, F. (2018). Mathematical homogenization of inelastic dissipative materials: a survey and recent progress. *Continuum Mechanics and Thermodynamics*, 30:1–51.

Chatzigeorgiou, G., Javili, A., and Steinmann, P. (2015). Multiscale modelling for composites with energetic interfaces at the micro- or nanoscale. *Mathematics and Mechanics of Solids*, 20:1130–1145.

Chatzigeorgiou, G., Meraghni, F., and Javili, A. (2017). Generalized interfacial energy and size effects in composites. *Journal of the Mechanics and Physics of Solids*, 106:257–282.

Chen, T., Chiu, M. S., and Weng, C. N. (2006). Derivation of the generalized Young-Laplace equation of curved interfaces in nanoscaled solids. *Journal of Applied Physics*, 100:074308.

Chhapadia, P., Mohammadi, P., and Sharma, P. (2011). Curvature-dependent surface energy and implications for nanostructures. *Journal of the Mechanics and Physics of Solids*, 59:2103–2115.

Christensen, R. M. and Lo, K. H. (1979). Solutions for effective shear properties in three phase sphere and cylinder models. *Journal of the Mechanics and Physics of Solids*, 27:315–330.

Cordero, N. M., Forest, S., and Busso, E. P. (2016). Second strain gradient elasticity of nano-objects. *Journal of the Mechanics and Physics of Solids*, 97:92–124.

Daher, N. and Maugin, G. A. (1986). The method of virtual power in continuum mechanics application to media presenting singular surfaces and interfaces. *Acta Mechanica*, 60:217–240.

Davydov, D., Javili, A., and Steinmann, P. (2013). On molecular statics and surface-enhanced continuum modeling of nano-structures. *Computational Materials Science*, 69:510–519.

dell'Isola, F. and Romano, A. (1987). On the derivation of thermomechanical balance equations for continuous system with a nonmaterial interface. *International Journal of Engineering Science*, 25:1459–1468.

Despringre, N., Chemisky, Y., Bonnay, K., and Meraghni, F. (2016). Micromechanical modeling of damage and load transfer in particulate composites with partially debonded interface. *Composite Structures*, 155:77–88.

Dimitri, R., Trullo, M., De Lorenzis, L., and Zavarise, G. (2015). Coupled cohesive zone models for mixed-mode fracture: A comparative study. *Engineering Fracture Mechanics*, 148:145–179.

Dingreville, R., Hallil, A., and Berbenni, S. (2014). From coherent to incoherent mismatched interfaces: A generalized continuum formulation of surface stresses. *Journal of the Mechanics and Physics of Solids*, 72:40–60.

Dingreville, R. and Qu, J. (2008). Interfacial excess energy, excess stress and excess strain in elastic solids: Planar interfaces. *Journal of the Mechanics and Physics of Solids*, 56:1944–1954.

Dinzart, F. and Sabar, H. (2017). New micromechanical modeling of the elastic behavior of composite materials with ellipsoidal reinforcements and imperfect interfaces. *International Journal of Solids and Structures*, 108:254–262.

Duan, H. L. and Karihaloo, B. L. (2007). Effective thermal conductivities of heterogeneous media containing multiple imperfectly bonded inclusions. *Physical Review B*, 75:064206.

Duan, H. L., Wang, J., Huang, Z. P., and Karihaloo, B. L. (2005). Size-dependent effective elastic constants of solids containing nano-inhomogeneities with interface stress. *Journal of the Mechanics and Physics of Solids*, 53:1574–1596.

Duan, H. L., Wang, J., and Karihaloo, B. L. (2009). Theory of Elasticity at the Nanoscale. *Advances in Applied Mechanics*, 42:1–68.

Duan, H. L., Yi, X., Huang, Z. P., and Wang, J. (2007). A unified scheme for prediction of effective moduli of multiphase composites with interface effects. Part I: Theoretical framework. *Mechanics of Materials*, 39:81–93.

Dugdale, D. S. (1960). Yielding of steel sheets containing slits. *Journal of the Mechanics and Physics of Solids*, 8:100–104.

Elsner, B. A. M., Müller, S., Bargmann, S., and Weissmüller, J. (2017). Surface excess elasticity of gold: Ab initio coefficients and impact on the effective elastic response of nanowires. *Acta Materialia*, 124:468–477.

Entchev, P. B. and Lagoudas, D. C. (2002). Modeling porous shape memory alloys using micromechanical averaging techniques. *Mechanics of Materials*, 34:1–24.

Fagerström, M. and Larsson, R. (2006). Theory and numerics for finite deformation fracture modelling using strong discontinuities. *International Journal for Numerical Methods in Engineering*, 66:911–948.

Fedotov, A. (2018). Interface model of homogenization for analysing the influence of inclusion size on the elastic properties of composites. *Composites Part B: Engineering*, 152:241–247.

Firooz, S., Chatzigeorgiou, G., Meraghni, F., and Javili, A. (2019a). Bounds on size effects in composites via homogenization accounting for general interfaces. *Continuum Mechanics and Thermodynamics*.

Firooz, S. and Javili, A. (2019). Understanding the role of general interfaces in the overall behavior of composites and size effects. *Computational Materials Science*, 162:245–254.

Firooz, S., Saeb, S., Chatzigeorgiou, G., Meraghni, F., Steinmann, P., and Javili, A. (2019b). Systematic study of homogenization and the utility of circular simplified representative volume element. *Mathematics and Mechanics of Solids*, 24:2961–2985.

Fried, E. and Gurtin, M. E. (2007). Thermomechanics of the interface between a body and its environment. *Continuum Mechanics and Thermodynamics*, 19:253–271.

Fried, E. and Todres, R. E. (2005). Mind the gap: The shape of the free surface of a rubber-like material in proximity to a rigid contactor. *Journal of Elasticity*, 80:97–151.

Fritzen, F. and Leuschner, M. (2015). Nonlinear reduced order homogenization of materials including cohesive interfaces. *Computational Mechanics*, 56:131–151.

Gasser, T. C. and Holzapfel, G. A. (2003). Geometrically non-linear and consistently linearized embedded strong discontinuity models for 3D

problems with an application to the dissection analysis of soft biological tissues. *Computer Methods in Applied Mechanics and Engineering*, 192:5059–5098.

Gitman, I. M., Askes, H., and Aifantis, E. C. (2005). The representative volume size in static and dynamic micro-macro transitions. *International Journal of Fracture*, 135:3–9.

Goudarzi, M. and Simone, A. (2019). Fiber neutrality in fiber-reinforced composites: Evidence from a computational study. *International Journal of Solids and Structures*, 156-157:14–28.

Gu, S. T., Liu, J. T., and He, Q. C. (2014). Size-dependent effective elastic moduli of particulate composites with interfacial displacement and traction discontinuities. *International Journal of Solids and Structures*, 51:2283–2296.

Gu, S. T., Monteiro, E., and He, Q. C. (2011). Coordinate-free derivation and weak formulation of a general imperfect interface model for thermal conduction in composites. *Composites Science and Technology*, 71:1209–1216.

Gurtin, M. E. and Murdoch, A. I. (1975). A continuum theory of elastic material surfaces. *Archive for Rational Mechanics and Analysis*, 57:291–323.

Hashin, Z. (1962). The Elastic Moduli of Heterogeneous Materials. *Journal of Applied Mechanics*, 29:143–150.

Hashin, Z. (1991). Thermoelastic Properties of particulate composites with impefect interface. *Journal of the Mechanics and Physics of Solids*, 39:745–762.

Hashin, Z. (2001). Thin interphase/imperfect interface in conduction. *Journal of Applied Physics*, 89:2261–2267.

Hashin, Z. (2002). Thin interphase/imperfect interface in elasticity with application to coated fiber composites. *Journal of the Mechanics and Physics of Solids*, 50:2509–2537.

Hashin, Z. and Rosen, B. W. (1964). The elastic moduli of fiber-reinforced materials. *Journal of Applied Mechanics*, 31:223–232.

He, J. and Lilley, C. M. (2008). Surface effect on the elastic behavior of static bending nanowires. *Nano Letters*, 8:1798–1802.

Hill, R. (1963). Elastic properties of reinforced solids: Some theoretical principles. *Journal of the Mechanics and Physics of Solids*, 11:357–372.

Hill, R. (1972). On Constitutive Macro-Variables for Heterogeneous Solids at Finite Strain. *Proceedings of the Royal Society A*, 326:131–147.

Huang, Z. P. and Sun, L. (2007). Size-dependent effective properties of a heterogeneous material with interface energy effect: from finite deformation theory to infinitesimal strain analysis. *Acta Mechanica*, 190:151–163.

Huang, Z. P. and Wang, J. (2006). A theory of hyperelasticity of multi-phase media with surface/interface energy effect. *Acta Mechanica*, 182:195–210.

Javili, A. (2017). Variational formulation of generalized interfaces for finite deformation elasticity. *Mathematics and Mechanics of Solids*, 23:303–322.

Javili, A. (2018). A note on traction continuity across an interface in a geometrically non-linear framework. *Mathematics and Mechanics of Solids*.

Javili, A., dell'Isola, F., and Steinmann, P. (2013a). Geometrically nonlinear higher-gradient elasticity with energetic boundaries. *Journal of the Mechanics and Physics of Solids*, 61:2381–2401.

Javili, A., Mcbride, A., Mergheim, J., Steinmann, P., and Schmidt, U. (2013b). Micro-to-macro transitions for continua with surface structure at the microscale. *International Journal of Solids and Structures*, 50:2561–2572.

Javili, A., McBride, A., and Steinmann, P. (2013c). Thermomechanics of Solids With Lower-Dimensional Energetics: On the Importance of Surface, Interface, and Curve Structures at the Nanoscale. A Unifying Review. *Applied Mechanics Reviews*, 65:010802.

Javili, A., Steinmann, P., and Mosler, J. (2017). Micro-to-macro transition accounting for general imperfect interfaces. *Computer Methods in Applied Mechanics and Engineering*, 317:274–317.

Kanouté, P., Boso, D. P., Chaboche, J. L., and Schrefler, B. A. (2009). Multiscale methods for composites: A review. *Archives of Computational Methods in Engineering*, 16:31–75.

Khisaeva, Z. F. and Ostoja-Starzewski, M. (2006). On the size of RVE in finite elasticity of random composites. *Journal of Elasticity*, 85:153–173.

Klarbring, A. (1991). Derivation of a model of adhesively bonded joints by the asymptotic expansion method. *International Journal of Engineering Science*, 29:493–512.

Koutsawa, Y., Karatrantos, A., Yu, W., and Ruch, D. (2018). A micromechanics approach for the effective thermal conductivity of composite materials with general linear imperfect interfaces. *Composite Structures*, 200:747–756.

Kushch, V. I., Mogilevskaya, S. G., Stolarski, H. K., and Crouch, S. L. (2013). Elastic fields and effective moduli of particulate nanocomposites with the Gurtin-Murdoch model of interfaces. *International Journal of Solids and Structures*, 50:1141–1153.

Levitas, V. I. and Samani, K. (2011). Size and mechanics effects in surface-induced melting of nanoparticles. *Nature Communications*, 2:284–286.

Liu, J.-T., Xie, F.-Y., He, Q.-C., Tang, S.-L., and Xiao, C.-W. (2019). Effective elastic isotropic moduli of highly filled particulate composites with arbitrarily shaped inhomogeneities. *Mechanics of Materials*, 135:35–45.

Liu, L., Yu, M., Lin, H., and Foty, R. (2017). Deformation and relaxation of an incompressible viscoelastic body with surface viscoelasticity. *Journal of the Mechanics and Physics of Solids*, 98:309–329.

Matouš, K., Geers, M. G. D., Kouznetsova, V. G., and Gillman, A. (2017). A review of predictive nonlinear theories for multiscale modeling of heterogeneous materials. *Journal of Computational Physics*, 330:192–220.

Moeckel, G. P. (1975). Thermodynamics of an interface. *Archive for Rational Mechanics and Analysis*, 57:255–280.

Moës, N. and Belytschko, T. (2002). Extended finite element method for cohesive crack growth. *Engineering Fracture Mechanics*, 69:813–833.

Mogilevskaya, S. G., Crouch, S. L., and Stolarski, H. K. (2008). Multiple interacting circular nano-inhomogeneities with surface/interface effects. *Journal of the Mechanics and Physics of Solids*, 56:2298–2327.

Monchiet, V. and Bonnet, G. (2010). Interfacial models in viscoplastic composites materials. *International Journal of Engineering Science*, 48:1762–1768.

Monteiro, E., He, Q. C., and Yvonnet, J. (2011). Hyperelastic large deformations of two-phase composites with membrane-type interface. *International Journal of Engineering Science*, 49:985–1000.

Murdoch, A. I. (1976). A thermodynamical theory of elastic material interfaces. *Quarterly Journal of Mechanics and Applied Mathematics*, 29:245–275.

Nazarenko, L., Bargmann, S., and Stolarski, H. (2017). Closed-form formulas for the effective properties of random particulate nanocomposites with complete Gurtin–Murdoch model of material surfaces. *Continuum Mechanics and Thermodynamics*, 29:77–96.

Needleman, A. (1987). A Continuum Model for Void Nucleation by Inclusion Debonding. *Journal of Applied Mechanics*, 54:525–531.

Ogden, R. W. (1974). On the overall moduli of non-linear elastic composite materials. *Journal of the Mechanics and Physics of Solids*, 22:541–553.

Olsson, P. A. T. and Park, H. S. (2012). On the importance of surface elastic contributions to the flexural rigidity of nanowires. *Journal of the Mechanics and Physics of Solids*, 60:2064–2083.

Ortiz, M. and Pandolfi, A. (1999). Finite-Deformation Irreversible Cohesive Elements for Three-Dimensional Crack-Propagation Analysis. *International Journal for Numerical Methods in Engineering*, 1282:1267–1282.

Park, H. S. and Klein, P. A. (2008). Surface stress effects on the resonant properties of metal nanowires: The importance of finite deformation kinematics and the impact of the residual surface stress. *Journal of the Mechanics and Physics of Solids*, 56:3144–3166.

Park, K. and Paulino, G. H. (2011). Cohesive Zone Models: A Critical Review of Traction-Separation Relationships Across Fracture Surfaces. *Applied Mechanics Reviews*, 64:060802.

Park, K., Paulino, G. H., and Roesler, J. R. (2009). A unified potential-based cohesive model of mixed-mode fracture. *Journal of the Mechanics and Physics of Solids*, 57:891–908.

Pham Huy, H. and Sanchez-Palencia, E. (1974). Phénomènes de transmission à travers des couches minces de conductivité Élevée. *Journal of*

Mathematical Analysis and Applications, 47:284–309.

Pindera, M. J., Khatam, H., Drago, A. S., and Bansal, Y. (2009). Micromechanics of spatially uniform heterogeneous media: A critical review and emerging approaches. *Composites Part B: Engineering*, 40:349–378.

Qian, J., Lin, J., Xu, G. K., Lin, Y., and Gao, H. (2017). Thermally assisted peeling of an elastic strip in adhesion with a substrate via molecular bonds. *Journal of the Mechanics and Physics of Solids*, 101:197–208.

Remmers, J. J. C., de Borst, R., and Needleman, A. (2008). The simulation of dynamic crack propagation using the cohesive segments method. *Journal of the Mechanics and Physics of Solids*, 56:70–92.

Saeb, S., Steinmann, P., and Javili, A. (2016). Aspects of Computational Homogenization at Finite Deformations: A Unifying Review From Reuss' to Voigt's Bound. *Applied Mechanics Reviews*, 68:050801.

Sanchez-Palencia, E. (1970). Comportement limite d'un probléme de transmissioná travers une plaque faiblement conductrice. *Comptes Rendus Mathématique Académie des Sciences*, 270:1026–1028.

Sevostianov, I., Mogilevskaya, S. G., and Kushch, V. I. (2019). Maxwell's methodology of estimating effective properties: Alive and well. *International Journal of Engineering Science*, 140:35–88.

Sharma, P. (2004). Size-dependent elastic fields of embedded inclusions in isotropic chiral solids. *International Journal of Solids and Structures*, 41:6317–6333.

Sharma, P. and Ganti, S. (2004). Size-Dependent Eshelby's Tensor for Embedded Nano-Inclusions Incorporating Surface-Interface Energies. *Journal of Applied Mechanics*, 71:663–671.

Sharma, P. and Wheeler, L. T. (2007). Size-Dependent Elastic State of Ellipsoidal Nano-Inclusions Incorporating Surface-Interface Tension. *Journal of Applied Mechanics*, 74:447–454.

Steigmann, D. J. and Ogden, R. W. (1999). Elastic surface substrate interactions. *Proceedings of the Royal Society of London A*, 455:437–474.

Temizer, I. and Zohdi, T. I. (2007). A numerical method for homogenization in non-linear elasticity. *Computational Mechanics*, 40:281–298.

Tian, L. and Rajapakse, R. K. N. D. (2007). Analytical Solution for Size-Dependent Elastic Field of a Nanoscale Circular Inhomogeneity. *Journal of Applied Mechanics*, 74:568–574.

van den Bosch, M. J., Schreurs, P. J. G., and Geers, M. G. D. (2006). An improved description of the exponential Xu and Needleman cohesive zone law for mixed-mode decohesion. *Engineering Fracture Mechanics*, 73:1220–1234.

Wang, G., Chen, Q., He, Z., and Pindera, M. J. (2018). Homogenized moduli and local stress fields of unidirectional nano-composites. *Composites Part B: Engineering*, 138:265–277.

Wang, J., Duan, H. L., Zhang, Z., and Huang, Z. P. (2005). An anti-interpenetration model and connections between interphase and interface models in particle-reinforced composites. *International Journal of Mechanical Sciences*, 47:701–718.

Wang, Z., Oelkers, R. J., Lee, K. C., and Fisher, F. T. (2016a). Annular Coated Inclusion model and applications for polymer nanocomposites Part I: Spherical inclusions. *Mechanics of Materials*, 101:170–184.

Wang, Z., Oelkers, R. J., Lee, K. C., and Fisher, F. T. (2016b). Annular Coated Inclusion model and applications for polymer nanocomposites Part II: Cylindrical inclusions. *Mechanics of Materials*, 101:50–60.

Wang, Z. Q., Zhao, Y. P., and Huang, Z. P. (2010). The effects of surface tension on the elastic properties of nano structures. *International Journal of Engineering Science*, 48:140–150.

Wells, G. N. and Sluys, L. J. (2001). A new method for modelling cohesive cracks using finite elements. *International Journal for Numerical Methods in Engineering*, 50:2667–2682.

Wu, C., Gowrishankar, S., Huang, R., and Liechti, K. M. (2016). On determining mixed-mode traction–separation relations for interfaces. *International Journal of Fracture*, 202:1–19.

Yvonnet, J., Quang, H. L., and He, Q. C. (2008). An XFEM/level set approach to modelling surface/interface effects and to computing the size-dependent effective properties of nanocomposites. *Computational Mechanics*, 42:119–131.

Zemlyanova, A. Y. and Mogilevskaya, S. G. (2018). On Spherical Inhomogeneity With Steigmann–Ogden Interface. *Journal of Applied Mechanics*, 85:121009.

Zhong, Z. and Meguid, S. A. (1997). On the Elastic Field of a Spherical Inhomogeneity with an Imperfectly Bonded Interface. *Journal of Elasticity*, 46:91–113.